

Global characteristics of GRBs observed with *INTEGRAL* and the inferred large population of low-luminosity GRBs[★]

S. Foley¹, S. McGlynn¹, L. Hanlon¹, S. McBreen², and B. McBreen¹

¹ UCD School of Physics, University College Dublin, Dublin 4, Ireland

² Max-Planck-Institut für extraterrestrische Physik, 85748 Garching, Germany

Received/Accepted

ABSTRACT

Context. *INTEGRAL* has two sensitive gamma-ray instruments that have detected and localised 47 gamma-ray bursts (GRBs) from its launch in October 2002 up to July 2007.

Aims. We present the spectral, spatial, and temporal properties of the bursts in the *INTEGRAL* GRB catalogue using data from the imager, IBIS, and spectrometer, SPI.

Methods. Spectral properties of the GRBs are determined using power-law and, where appropriate, Band model and quasithermal model fits to the prompt emission. Spectral lags, i.e. the time delay in the arrival of low-energy γ -rays with respect to high-energy γ -rays, are measured for 31 of the GRBs.

Results. The photon index distribution of power-law fits to the prompt emission spectra is presented and is consistent with that obtained by *Swift*. The peak flux distribution shows that *INTEGRAL* detects proportionally more weak GRBs than *Swift* because of its higher sensitivity in a smaller field of view. The all-sky rate of GRBs above ~ 0.15 ph cm⁻² s⁻¹ is ~ 1400 yr⁻¹ in the fully coded field of view of IBIS. Two groups are identified in the spectral lag distribution of *INTEGRAL* GRBs, one with short lags < 0.75 s (between 25–50 keV and 50–300 keV) and one with long lags > 0.75 s. Most of the long-lag GRBs are inferred to have low redshifts because of their long spectral lags, their tendency to have low peak energies, and their faint optical and X-ray afterglows. They are mainly observed in the direction of the supergalactic plane with a quadrupole moment of $Q = -0.225 \pm 0.090$ and hence reflect the local large-scale structure of the Universe.

Conclusions. The spectral, spatial, and temporal properties of the 47 GRBs in the *INTEGRAL* catalogue are presented and compared with the results from other missions. The rate of long-lag GRBs with inferred low luminosity is $\sim 25\%$ of Type Ib/c supernovae. Some of these bursts could be produced by the collapse of a massive star without a supernova. Alternatively, they could result from a different progenitor, such as the merger of two white dwarfs or a white dwarf with a neutron star or black hole, possibly in the cluster environment without a host galaxy.

Key words. gamma rays: bursts

1. Introduction

The prompt emission of gamma-ray bursts provides valuable insight into the mechanisms from which these extremely explosive events originate. Their short durations and highly variable temporal structures provide constraints on the physics of the central engine powering the burst. A number of GRB reviews have been published (e.g. Zhang & Mészáros 2004; Piran 2005; Mészáros 2006). In recent years, the advent of missions such as the Compton Gamma-Ray Observatory (CGRO) (Fishman & Meegan 1995), along with the improved imaging capabilities of missions such as *BeppoSAX* (Boella et al. 1997), HETE II (Sakamoto et al. 2005), *INTEGRAL* (Winkler et al. 2003), and *Swift* (Gehrels et al. 2004), has led to the precise localisations of GRBs and enabled rapid multi-wavelength follow-up observations. The X-ray, optical and radio afterglow detections are listed in Table 1 for a total of 423 GRBs well localised by these missions between July

Table 1. Afterglow detections for GRBs localised by recent γ -ray missions between July 1996 and July 2007.

	<i>BeppoSAX</i>	HETE II	<i>INTEGRAL</i>	<i>Swift</i>
GRBs	55	79	47	242
X-ray	31	19	17	209
Optical	17	30	16	123
Radio	11	8	8	17

1996 and July 2007, showing in particular the observed number of afterglows based on *INTEGRAL* GRB detections. The data are taken from the webpage maintained by Jochen Greiner¹.

There are two main γ -ray instruments on board *INTEGRAL*, namely IBIS (Ubertini et al. 2003) and SPI (Vedrenne et al. 2003), optimised for high-resolution imaging and spectroscopy of the γ -ray sky, respectively. The IBIS instrument is comprised of two separate layers of detectors, ISGRI in the 15 keV–1 MeV energy range (Lebrun et al. 2003), and PICsIT in the 180 keV–10 MeV energy range (Labanti et al. 2003). IBIS/ISGRI has 16384 CdTe detectors, located 3.4 m from a tungsten mask which projects a shadowgram on the detector plane. Maps of

Send offprint requests to: S. Foley, e-mail: sfoley@bermuda.ucd.ie

[★] Based on observations with *INTEGRAL*, an ESA project with instruments and science data centre funded by ESA member states (especially the PI countries: Denmark, France, Germany, Italy, Switzerland, Spain), Czech Republic and Poland, and with the participation of Russia and the USA.

¹ <http://www.mpe.mpg.de/~jcg/grbgen.html>.

the sky are reconstructed by decoding the shadowgram with the mask pattern. IBIS has a fully coded field of view (FCFoV) of $9^\circ \times 9^\circ$ and a partially coded field of view (PCFoV) of $19^\circ \times 19^\circ$ at 50% coding and $29^\circ \times 29^\circ$ at zero coding. SPI consists of 19 hexagonal germanium (Ge) detectors covering the energy range 20 keV–8 MeV with high energy resolution of 2.5 keV at 1.3 MeV. A coded mask is located 1.71 m above the detector plane for imaging purposes, giving a 16° corner-to-corner FCFoV and a PCFoV of 34° . The SPI and IBIS instruments are supported by an optical camera (OMC, Mas-Hesse et al. (2003)) and an X-ray monitor (JEM-X, Lund et al. (2003)).

The *INTEGRAL* Burst Alert System (IBAS², Mereghetti et al. (2003b)) is an automatic ground-based system for the accurate localisation of GRBs and the rapid distribution of GRB coordinates, providing, on average, 0.8 GRBs per month with an error radius of ~ 3 arcminutes. *INTEGRAL* has detected 46 long-duration GRBs ($T_{90} \gtrsim 2$ s) and 1 short-duration GRB ($T_{90} \lesssim 2$ s) between October 2002 and July 2007. *INTEGRAL* bursts of particular interest include the low-luminosity GRB 031203 (Sazonov et al. 2004), the very intense GRB 041219a (McBreen et al. 2006), a number of X-ray rich GRBs such as GRB 040223 (McGlynn et al. 2005; Filliatre et al. 2006), GRB 040403 (Mereghetti et al. 2005) and GRB 040624 (Filliatre et al. 2006), and the short-duration GRB 070707 (McGlynn et al. 2008a). In addition, Marcinkowski et al. (2006) have detected a bright, hard GRB outside the field of view using the ISGRI Compton mode. Spectroscopic redshifts have been determined for four *INTEGRAL* GRBs, i.e. GRB 031203 at $z=0.1055$ (Prochaska et al. 2004); GRB 050223 at $z=0.584$ (Pellizza et al. 2006); GRB 050525a at $z=0.606$ (Foley et al. 2005) and GRB 050502a at $z=3.793$ (Prochaska et al. 2005). Non-spectroscopic redshifts have been inferred for GRB 040812 ($0.3 < z < 0.7$, D’Avanzo et al. (2006)) and GRB 040827 ($0.5 < z < 1.7$, de Luca et al. (2005)). The low efficiency for measuring redshifts is partially due to the fact that *INTEGRAL* spends a large amount of observing time pointing towards the galactic plane.

Gamma-ray burst continuum spectra are in most cases well described by a smoothly broken power law in the 30 keV–2 MeV energy range (Band et al. 1993). The γ -ray spectral shape as predicted for optically thin synchrotron emission are two asymptotically broken power laws but many GRBs are not consistent with this model and it requires modification to fit the observed spectra (e.g. Lloyd-Ronning & Petrosian 2002). It has been proposed that GRB spectra may contain a thermal component (e.g. Ghirlanda et al. 2003; Ryde 2005; Kaneko et al. 2006; McBreen et al. 2006). The interpretation of quasithermal emission as opposed to synchrotron emission can provide an explanation for the observed spectral characteristics within a more physical framework (e.g. Rees & Mészáros 2005; Ryde et al. 2006).

The time profiles of GRBs often exhibit a complex and unpredictable nature, displaying considerable diversity both in terms of structure and duration (McBreen et al. 2001; Quilligan et al. 2002). This makes them difficult to classify on the basis of temporal structure alone. One notable feature of GRB time profiles is the tendency for emission in a high-energy band to lead the arrival of photons in a low-energy band (e.g. Cheng et al. 1995; Wu & Fenimore 2000; Norris et al. 2000; Bolmont et al. 2006; McBreen et al. 2006; Hakkila et al. 2007, 2008). The energy-dependent lag allows the temporal

and spectral properties of the GRB prompt γ -ray emission to be combined in a single measurement. The typical lag values measured for long-duration GRBs detected by the Burst and Transient Source Experiment (BATSE) between the 25–50 keV and 100–300 keV channels concentrate ~ 100 ms (Norris et al. 2000). An anti-correlation between spectral lag and isotropic peak luminosity was first observed by Norris et al. (2000), using 6 BATSE bursts with measured redshifts. A similar trend is observed between lag and luminosity for a number of *Swift* GRBs of known redshift (Gehrels et al. 2006). However, there exist notable outliers, in particular the ultra-low luminosity bursts GRB 980425, GRB 031203 and GRB 060218, associated with the supernovae SN 1998bw, SN 2003lw and SN 2006aj, respectively. Short bursts ($T_{90} < 2$ s) have very small or negligible lags (Yi et al. 2006; Norris & Bonnell 2006; Zhang et al. 2006a) and relatively low peak luminosities and so do not lie on the correlation (Gehrels et al. 2006). On this basis, the spectral lag has been suggested by Donaghy et al. (2006) as one of the criteria to determine whether a burst is long or short. Pulse width and spectral lag are strongly related, with wider pulses tending to have longer spectral lags (Norris & Bonnell 2006). Relative spectral lags, defined as the ratio of spectral lag to pulse width, have been found to have normal distributions centering on ~ 100 ms for long bursts (Zhang et al. 2006b) and ~ 14 ms for short GRBs (Zhang et al. 2006a). The lag-luminosity and $E_{\text{peak}}-E_{\text{iso}}$ (Amati et al. 2007) relationships can be used as distance indicators for GRBs (Schaefer 2007), provided the role of selection effects is understood and quantified (e.g. Butler et al. 2008).

The physical basis underlying spectral lags is not yet well understood (Schaefer 2004). The observed lag of a burst is a direct consequence of its spectral evolution because the peak of the νF_ν spectrum, E_{peak} , decays with time (Kocevski & Liang 2003; Hafizi & Mochkovitch 2007). The internal shock model allows for three possible sources of temporal variations in GRB pulses: cooling, hydrodynamics and geometric angular effects. Cooling is unable to fully account for the time lag since the synchrotron timescale is much shorter than the lag timescale (Wu & Fenimore 2000). It has been proposed that the lag-luminosity relation may arise kinematically, based on the viewing angle at which the GRB jet is observed (Salmonson 2000). In this interpretation, a high-luminosity GRB with short spectral lag corresponds to a jet with a small viewing angle, while a low-luminosity GRB with long spectral lag corresponds to a jet with a large viewing angle (Ioka & Nakamura 2001). A correlation has also been observed between spectral lag (or luminosity) and jet-break time, thereby connecting the prompt and afterglow phases of GRBs. This may be understood in terms of a model in which the Lorentz factor decreases away from the axis of the GRB jet (Salmonson & Galama 2002). The connection between spectral lag and the timescales involved in the hydrodynamic processes and radiative mechanisms of the burst has been discussed by Daigne & Mochkovitch (2003).

A subpopulation of local, faint, long-lag GRBs has been suggested by Norris (2002) from a study of BATSE bursts, which implies that events with low peak fluxes (F_{Peak} (50–300 keV) ~ 0.25 ph cm⁻² s⁻¹) should be predominantly long-lag GRBs. The sensitivity of IBIS is such that bursts fainter than the BATSE limit can be well localised. In this paper we present the spectral, spatial and temporal lag properties of the complete sample of the 47 GRBs detected in the field of view of IBIS and SPI up to July 2007. Section 2 describes the capabilities of SPI’s anti-coincidence shield as a GRB detector. The spectral and lag analyses are described in Sect. 3 and results are presented in Sect. 4. Sections 5 and 6 discuss the significance of these results, which

² http://ibas.iasf-milano.inaf.it/IBAS_Results.html

imply a large population of long-lag GRBs with low luminosities. The cosmological parameters adopted throughout the paper are $H_0 = 70 \text{ km s}^{-1} \text{ Mpc}^{-1}$, $\Omega_m = 0.3$, $\Omega_{vac} = 0.7$. All errors are quoted at the 1σ confidence level.

2. GRBs detected with SPI's Anti-Coincidence Shield

In addition to SPI and IBIS, the Anti-Coincidence Shield (ACS) surrounding the SPI detectors works as a highly-sensitive GRB detector above $\sim 80 \text{ keV}$ but lacks spatial and spectral information (von Kienlin et al. 2003b). The ACS consists of 91 BGO crystals with a total mass of 512 kg surrounding SPI. It has a maximum sensitivity to GRBs at $\sim 90^\circ$ from the pointing direction and provides lightcurves in 50 ms intervals. The ACS detects GRBs at a rate of ~ 1 every 2–3 days. A selection of GRBs detected with SPI-ACS is shown in Fig. 1 using data taken from the publicly available catalogue of SPI-ACS GRBs³. Temporal analysis of a more complete sample is presented in Rau et al. (2005). The ACS is used as part of the interplanetary network (Hurley et al. 2006).

3. Analysis of GRBs observed with IBIS and SPI

3.1. Spectral Analysis

Spectral analysis of the GRBs was performed using *INTEGRAL*'s Online Software Analysis version 5.1 available from the *INTEGRAL Science Data Centre*⁴. The T_{90} duration (i.e., the time during which 5% to 95% of the GRB counts are recorded) was determined for each GRB in the 20–200 keV energy range and the spectrum was generated for that time interval. For cases in which the GRB had a multi-peaked time profile, the GRB was divided into its constituent pulses and a spectrum was generated for each pulse to investigate evolution of the spectral parameters during the burst.

Each GRB was fit by a simple power-law model, the Band model and a quasithermal (combined power-law + blackbody) model. Weak GRBs are best fit by a single power-law model because the limited statistics are insufficient to constrain any additional parameters. For brighter GRBs, the Band model or combined power-law + blackbody fits usually result in an improved χ^2 value. The peak flux was measured over the brightest 1 s time interval in the 20–200 keV energy range. The fluence of each GRB was determined for the T_{90} interval in the 20–200 keV energy range for the IBIS spectra, and the 20–200 keV and 20 keV–8 MeV energy ranges for the SPI spectra.

3.2. Spectral Lag Analysis

In order to measure the lag, background-subtracted lightcurves were extracted in three energy bands comparable to those used with BATSE, namely 25–50 keV (Channel 1), 50–100 keV (Channel 2) and 100–300 keV (Channel 3). The lag, τ , between two energy channels was determined by computing the cross-correlation function (CCF) between the two lightcurves as a function of temporal lag as described by Band (1997) and Norris et al. (2000). Assuming the time profiles in both energy channels display sufficient similarity, the peak in the CCF then corresponds to the time lag of the GRB between the two energy channels in question. The lag was determined between Channels

1 and 2, $\tau_{2,1}$, Channels 1 and 3, $\tau_{3,1}$, and to account for those cases in which the signal level in Channel 3 was insufficient to determine an accurate lag, the counts in Channels 2 and 3 were combined and correlated with Channel 1 to give $\tau_{2+3,1}$. In this paper, GRBs with $\tau_{2+3,1} > 0.75 \text{ s}$ are defined as long-lag.

The reliability of the cross-correlation technique was limited primarily by the signal to noise ratio of the data. The faint nature of many of the GRBs detected by *INTEGRAL* can result in a noisy CCF with an ambiguous peak. A denoising technique was used to smooth the lightcurve while retaining the structure of the burst. This technique involved filtering the signal to remove the high frequency components in order to produce a denoised lightcurve (Quilligan et al. 2002). The wavelet analysis was carried out on the weakest GRBs with F_{peak} (20–200 keV) $\lesssim 0.6 \text{ ph cm}^{-2} \text{ s}^{-1}$ using the wavelet toolbox in MATLAB. As an example, the lightcurves of GRB 070615 in the 25–50 keV and 50–300 keV energy bands are shown in Fig. 2(a) before and Fig. 2(b) after denoising. The CCFs resulting from the raw data and denoised data are plotted in Fig. 2(c). The denoised data results in a smoother CCF peak and a more significant correlation, while retaining the position of the peak at a similar lag value to that measured with the raw data. Six *INTEGRAL* GRBs were too weak for a reliable lag to be determined using either the raw or denoised data.

The CCF was fit with a fourth order polynomial in order to account for the asymmetry of the CCF (Norris et al. 2000). The peak of the polynomial fit to the CCF was then taken to be the true lag value. For each GRB, an average spectral lag over the total burst duration was determined. For the cases in which separate pulses could be clearly distinguished by eye, spectral lags were measured for the individual pulses to investigate the evolution of spectral lag during the burst. In each case, the spectral lag was determined for regions of the lightcurve above 10%, 30% and 50% of the peak count rate and over a number of different lag ranges to ensure that consistent results were obtained. The optimum lag range was taken to be that for which the CCF was concave down but short enough that the CCF peak was well fit. Statistical errors were calculated using a bootstrap method as described in Norris et al. (2000). This involves adding Poissonian noise based on the observed counts to the lightcurves in the different energy channels and re-computing the CCF in 100 realisations for each burst. The 50th ranked value is then the mean lag and the 16th and 84th ranked values represent $\pm 1\sigma$. The lightcurve data was over-resolved by a factor of 10 in order to compute the errors at a time resolution less than the natural binning of the raw data.

4. Results

The exposure map and spatial distribution of the 47 GRBs observed with IBIS are shown in galactic coordinates in Fig. 3 for the period from October 2002 to July 2007. The burst distribution is significantly concentrated towards the galactic plane, reflecting the direction in which the satellite is pointed. *INTEGRAL* spent 64% of its observing time in the half of the sky at galactic latitudes between $\pm 30^\circ$.

The properties of the 47 *INTEGRAL* GRBs are presented in Tables 6 and 3. The coordinates and afterglow information are taken from the webpage maintained by Jochen Greiner. The typical size of the *INTEGRAL* error box is $3'$. GRB 060428c did not trigger IBAS but was discovered during subsequent analysis of *INTEGRAL* archival data (Grebenev & Chelovekov 2007). The spectral lag for each burst is presented in Table 6, with 11 GRBs

³ <http://www.mpe.mpg.de/gamma/science/grb/1ACSburst.html>

⁴ <http://isdc.unige.ch/>

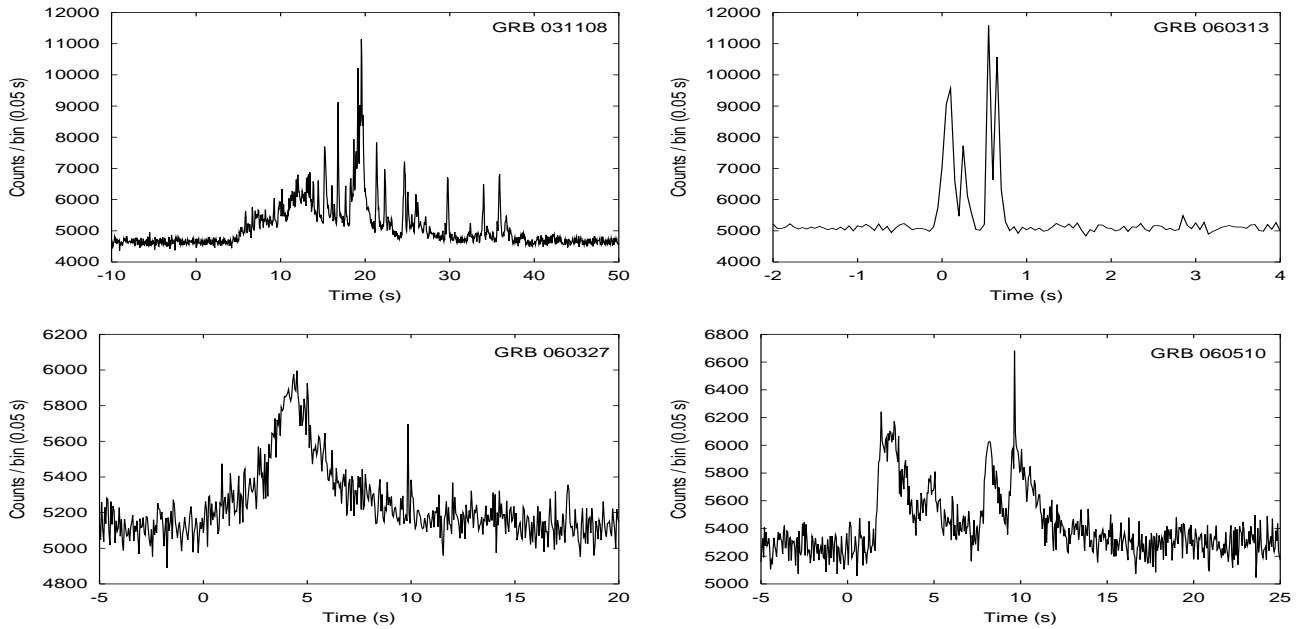


Fig. 1. A selection of GRB lightcurves detected by the Anti-Coincidence Shield at photon energies > 80 keV.

having long lags ($\tau_{2+3,1} > 0.75$ s). The off-axis angle distribution of the GRBs in the IBIS FoV is given in Fig. 4. The bursts have preferentially higher peak fluxes at larger angles outside the FCFoV of IBIS due to the reduced sensitivity at lower coding levels. The log N-log P distribution is given in Fig. 5 for all IBIS GRBs and separately for the small subsample of 11 long-lag GRBs. The long-lag GRBs appear to form a separate population at low values of P. The T_{90} distribution of *INTEGRAL* GRBs is shown in Fig. 6 and compared with the bimodal distribution for BATSE GRBs (Kouveliotou et al. 1993). There is reasonable agreement between the two distributions, especially when the small number of *INTEGRAL* GRBs is taken into account. The IBIS lightcurves of 43 *INTEGRAL* bursts are given in the Appendix in the 25–50 keV and 50–300 keV energy ranges. In general, the faint bursts have smooth, long-duration profiles with only one or two weak pulses.

4.1. Spectral Properties of *INTEGRAL* GRBs

The spectral information given in Table 6 is obtained from the IBIS detector, with the exception of GRB 041219a, GRB 050525a, GRB 060901 and GRB 061122 for which the peak flux and fluence values are measured with SPI in the 20–200 keV energy range due to telemetry gaps in the IBIS data (McBreen et al. 2006; McGlynn et al. 2008b). Limited spectral information is available for GRB 021125 due to significant telemetry loss while the satellite was in calibration mode (Malaguti et al. 2003). Data for GRB 060930 and GRB 070311 are currently not publicly available and values shown are taken from Gotz et al. (2006) and Mereghetti et al. (2007), respectively. Peak flux values are integrated over the brightest 1 second time interval in the 20–200 keV energy band and fluence values are measured over the same energy range. Photon indices are given for a power-law fit to the spectra in the 20–200 keV energy range. Spectral parameters obtained from IBIS and SPI spectra for which the Band model and quasithermal model are fit are listed in Table 3. The values obtained from a combined IBIS and SPI spectral fit to GRB 060428c over the 20–

400 keV energy range are taken from Grebenev & Chelovekov (2007). GRB 030131 and GRB 050502a were detected during a satellite slew so SPI spectral analysis was not possible for these bursts. A sample of *INTEGRAL* νF_ν spectra is shown in Fig. 7.

The distribution of photon indices is shown in Fig. 8 for *INTEGRAL* and *Swift* GRBs for which a power-law model was fit to the spectral data in the 20–200 keV and 15–150 keV energy ranges, respectively. In comparison to *Swift*, *INTEGRAL* detects proportionally more soft GRBs with steeper power-law photon indices.

Fig. 9 compares the peak flux (20–200 keV) distribution of the GRBs observed by IBIS (solid line) to the peak flux (15–150 keV) distribution of the GRBs detected by the BAT instrument on *Swift*. IBIS detects proportionally more weak GRBs than *Swift* because of its better sensitivity within a FoV that is smaller by a factor of ~ 12 .

4.2. Spectral Lags of *INTEGRAL* GRBs

The spectral lag results are presented in Table 6. A positive spectral lag follows the usual convention of high energy emission preceding low energy emission. The time intervals which were correlated to determine the spectral lags are marked with vertical lines on the lightcurves in the Appendix. Within these intervals, only those counts above 10% of the peak count rate were correlated to give the lag values in Table 6. The number distribution of spectral lags measured over the full burst duration is given in Fig. 10 for the 28 long-duration GRBs with a measured lag between Channel 1 (25–50 keV) and Channels 2 & 3 (50–300 keV). No statistically significant negative spectral lags are found. Negative lags, which violate the typical hard-soft evolution of GRBs, have been observed in a small minority of cases (e.g. Chen et al. 2005) and may be more prevalent in short bursts (Gupta et al. 2002; Yi et al. 2006). A long tail extending to ~ 5 s is observed in the lag distribution in Fig. 10 and a clear separation between short and long lag is drawn at $\tau_{2+3,1} \sim 0.75$ s. Thus, long-lag bursts have $\tau_{2+3,1} > 0.75$ s and those with $\tau_{2+3,1} < 0.75$ s are referred to as short-lag GRBs. The

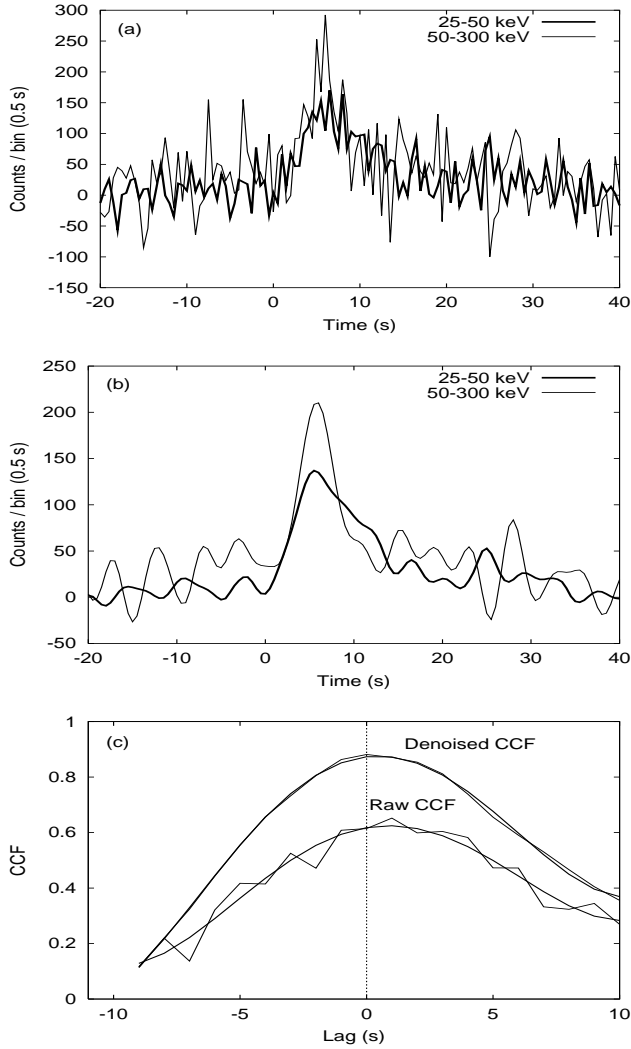


Fig. 2. (a) Raw and (b) denoised lightcurves of GRB 070615 in the 25–50 keV (dark line) and 50–300 keV (light line) energy bands. (c) Cross correlation functions and polynomial fits giving a lag of $0.40^{+0.15}_{-0.25}$ and $0.40^{+0.15}_{-0.20}$ for the raw and denoised lightcurve data, respectively. The dashed line represents a lag of 0 s.

11 long-lag GRBs are identified in Table 6, with 4 in the FCFoV, a further 4 in the PCFoV to the 50% coding level and the remaining 3 GRBs at larger off-axis angles (Fig. 4).

The spectral lag distribution of *INTEGRAL* GRBs as a function of peak flux is shown in Fig. 11. The BeppoSAX SN burst GRB 980425 (Galama et al. 1998) is also shown in Fig. 11. The SN burst XRF 060218, with a peak flux of $0.6 \text{ ph cm}^{-2} \text{ s}^{-1}$, is not included in the figure because it has an extremely long lag of $61 \pm 26 \text{ s}$ (Liang et al. 2006). The other low luminosity burst shown in Fig. 11 is GRB060505, which has no associated SN (Fynbo et al. 2006; McBreen et al. 2008). The figure shows that both bright and faint GRBs have short spectral lags, but there is an obvious absence of bright long-lag GRBs. Therefore GRBs with long spectral lags tend to be weak bursts with low peak flux. This trend is in good agreement with that observed using BATSE GRBs (Norris 2002), where the proportion of long-lag GRBs is negligible among bright BATSE bursts and increases to around 50% at the trigger threshold. Using 1429 BATSE GRBs, Norris (2002) identified three GRB groups that consist of bright short-

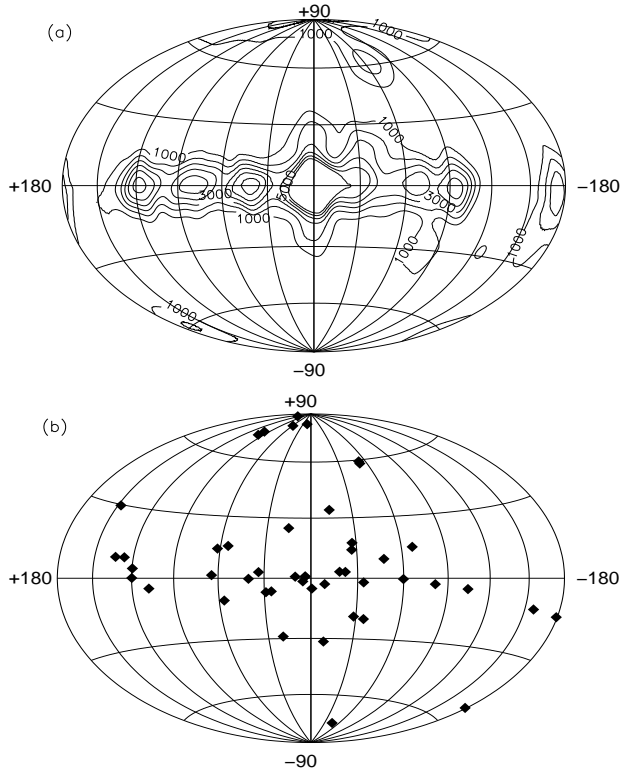


Fig. 3. (a) *INTEGRAL* exposure map in galactic coordinates from October 2002 up to July 2007 (contours in units of kiloseconds), showing the concentration of exposure in the direction of the galactic plane (Erik Kuulkers, private communication). (b) Spatial distribution of 47 *INTEGRAL* GRBs detected between October 2002 and July 2007 in galactic coordinates.

lag bursts, weak short-lag bursts and weak long-lag bursts. These groups are also clearly identifiable for the *INTEGRAL* sample in Fig. 11.

The isotropic peak luminosity as a function of spectral lag is shown in Fig. 12 and includes the 3 *INTEGRAL* GRBs with known redshift for which a lag was measured. The low-luminosity bursts GRB 980425, XRF 060218 and GRB 060505 are also plotted in Fig. 12. The dashed line is the anti-correlation between lag and luminosity proposed by Norris et al. (2000). The bright *INTEGRAL* bursts GRB 050502a and GRB 050525a have peak luminosities of $1.8 \times 10^{52} \text{ erg s}^{-1}$ and $1.8 \times 10^{51} \text{ erg s}^{-1}$ and spectral lags of $0.11^{+0.07}_{-0.06} \text{ s}$ and $0.130^{+0.003}_{-0.002} \text{ s}$, respectively and follow the trend of the relation. At $z = 0.106$, GRB 031203 has a peak luminosity of $8.4 \times 10^{48} \text{ erg s}^{-1}$ and spectral lag of $0.17^{+0.03}_{-0.04} \text{ s}$, causing it to fall significantly below the correlation (Sazonov et al. 2004; Gehrels et al. 2006). The HETE burst GRB 030528 has a long lag similar to that of GRB 980425 but a relatively high luminosity and is consistent with the lag-luminosity relation (Gehrels et al. 2006). A long spectral lag is therefore not an exclusive determinant for a low-luminosity GRB.

For the SN burst GRB 031203, spectral lags of $0.24 \pm 0.12 \text{ s}$ between 20–50 keV and 100–200 keV (Sazonov et al. 2004) and $0.30 \pm 0.20 \text{ s}$ between 15–50 keV and 50–150 keV (Shrader 2006) have been reported and are consistent with the value $\tau_{3,1} = 0.17^{+0.03}_{-0.04} \text{ s}$ in Table 6 and Fig. 11. A spectral lag for GRB 040403 of $0.6 \pm 0.1 \text{ s}$ between 15–40 keV and 40–200 keV has previously been reported (Mereghetti et al. 2005), consistent with the value of $\tau_{2+3,1} = 0.95^{+0.25}_{-0.15} \text{ s}$ in Table 6, taking into account

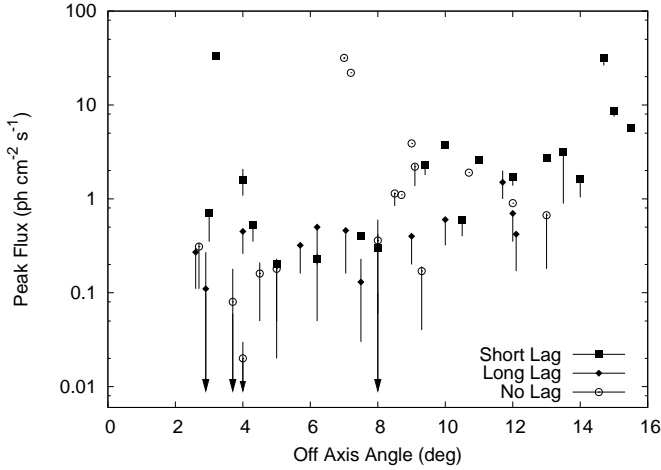


Fig. 4. The off-axis angle distribution of the GRBs in the IBIS FoV as a function of peak flux (20–200 keV). The FCFoV is $9^\circ \times 9^\circ$ and the boundary of the PCFoV is between 4.5° and 6.2° , depending on the azimuthal angle of the GRB position. The long-lag GRBs are marked with filled diamonds. There are 11 GRBs within the FCFoV and 4 have long lags. IBIS is less sensitive to γ -ray sources outside the FCFoV as reflected by the decrease in the number of faint GRBs.

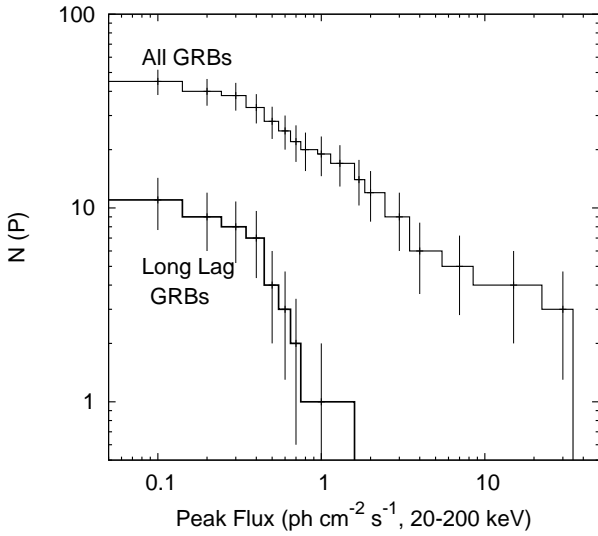


Fig. 5. The cumulative log N-log P distribution of the 47 GRBs detected by IBIS, with peak flux P measured between 20–200 keV. The distribution is biased by the lower sensitivity of IBIS at large off-axis angles (Fig. 4). The small subset of 11 long-lag GRBs is shown separately.

the different energy ranges. The spectral lag of GRB 050525a was found to be $\tau_{3,1} = 0.124 \pm 0.006$ s (Norris et al. 2005), in agreement with the value of $\tau_{3,1} = 0.130^{+0.003}_{-0.002}$ s obtained in Table 6. The spectral lag for the short burst, GRB 070707 is 5 ± 5 ms ($\tau_{2+3,1}$), consistent with the negligible lag values expected for short GRBs (Norris & Bonnell 2006; Zhang et al. 2006a). For most of the GRBs with distinct separate pulses, the spectral lag does not evolve significantly during the burst, i.e. GRB 030320, GRB 040106, GRB 040422, GRB 040812, GRB 050522 and GRB 050525a. Some evolution is evident in GRB 050918 for which the lag varies from $0.50^{+0.05}_{-0.04}$ s for the

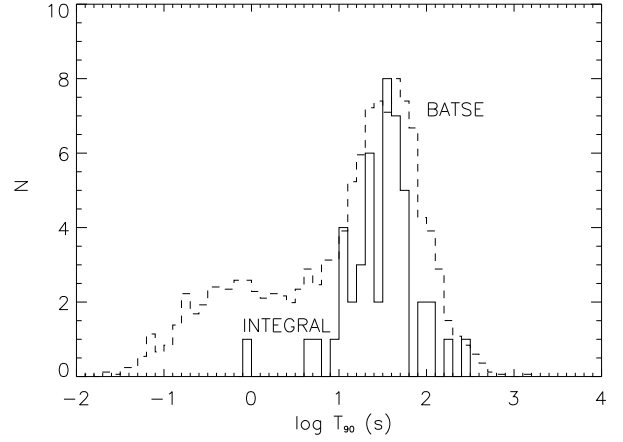


Fig. 6. T_{90} distribution of *INTEGRAL* GRBs (solid line) in comparison to that of *BATSE* (dashed line). The *BATSE* distribution is normalised to the peak of the *INTEGRAL* distribution for clarity. The *BATSE* data for 2041 GRBs is taken from the Current Catalog at <http://www.batse.msfc.nasa.gov/batse/grb/catalog/current>.

first pulse of the burst, to a slightly negative lag of -0.14 ± 0.01 s for the second pulse. For GRB 041219a, the lag of the precursor is relatively long and is much shorter for the main emission pulses, as discussed in McBreen et al. (2006). Spectral lag evolution is often seen in multi-peaked GRBs (e.g. Hakkila & Giblin 2004; Chen et al. 2005; Ryde et al. 2005; Hakkila et al. 2008), and poses obvious difficulties for the use of the lag as a luminosity indicator.

Spectral lags are measured between wavelet-smoothed lightcurves for a number of GRBs with F_{peak} (20–200 keV) ≤ 0.6 $\text{ph cm}^{-2} \text{s}^{-1}$ and are denoted by † in Table 6. Table 5 gives the lags determined with and without denoising for these GRBs. The denoising method allows the lag to be measured in some cases for very weak GRBs where it cannot be determined using the raw data and in most cases the lag is better constrained with smaller errors.

Spectral lag measurements were not possible for 16 GRBs for the following reasons:

1. Significant telemetry gaps occur in the IBIS data for GRB 021125 (Fig. A.1 (a)), GRB 030131, GRB 030227 (Fig. A.1 (c)) and GRB 061122 (Fig. A.4 (d)).
2. GRB 041015 (Fig. A.2 (f)), GRB 050129 (Fig. A.2 (i)), GRB 050922a (Fig. A.3 (g)), GRB 060114 (Fig. A.3 (j)), GRB 060204a (Fig. A.3 (l)) and GRB 060912b (Fig. A.4 (b)) are too weak, even when denoised lightcurves are used for the correlation.
3. GRB 050223 (Fig. A.2 (j)), GRB 050714a (Fig. A.3 (e)) and GRB 051105b (Fig. A.3 (h)) have significant temporal variations which results in incorrect pulses being correlated and so significant CCF peaks were not found for these bursts.
4. IBIS data are currently unavailable to this team for GRB 060428c, GRB 060930 and GRB 070311.

There are special circumstances for some GRBs and these include:

1. Spectral lags for GRB 021219 (Fig. A.1 (b)) and GRB 050502a (Fig. A.2 (k)) are measured over the region of the burst before telemetry saturation occurred.

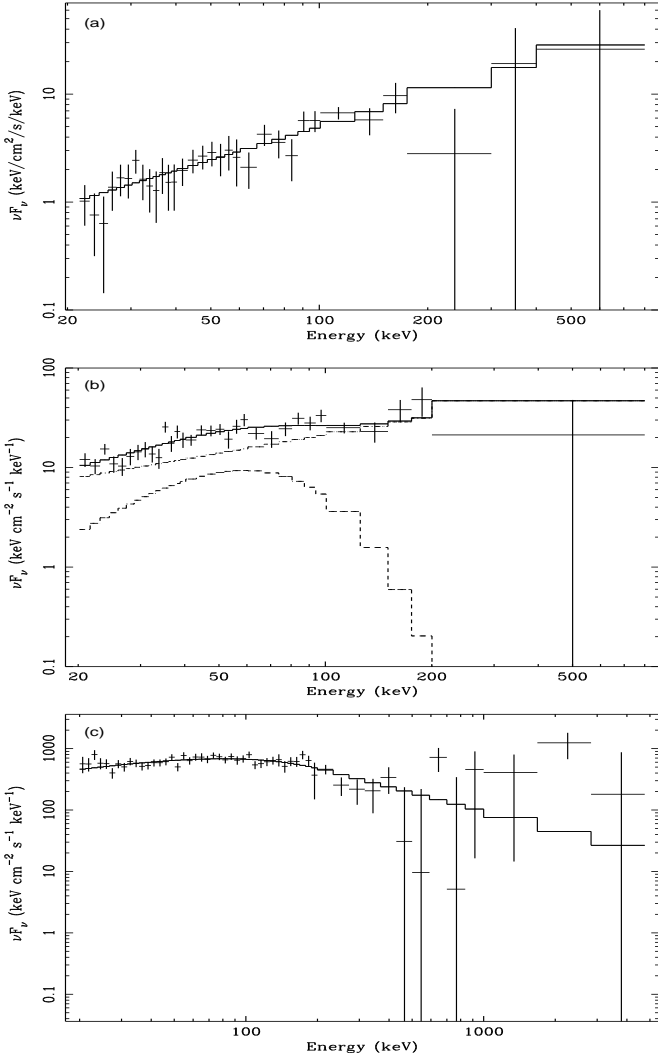


Fig. 7. (a) IBIS νF_ν power-law spectrum of GRB 060114 in the 20–800 keV energy range. (b) IBIS νF_ν spectrum of GRB 061025, fit by the quasithermal (blackbody + power-law) model in the 20–800 keV energy range. (c) SPI νF_ν spectrum of GRB 050525a, from 20 keV–8 MeV, fit with the Band model.

2. For GRB 030529 only the first peak is correlated because telemetry gaps occur in the later data (Fig. A.1 (f)).
3. GRB 040903 (Fig. A.2 (e)) and GRB 050522 (Fig. A.3 (b)) are not detected above 50 keV so the lag is determined between 15–25 keV and 25–50 keV (Channel 2).
4. GRB 041219a (Fig. A.2 (h)) (Fenimore et al. 2004) and GRB 050525a (Fig. A.3 (c)) were simultaneously observed by *INTEGRAL* and *Swift*. There are telemetry gaps in the IBIS data for both bursts and SPI data types do not permit energy-resolved lightcurves to be extracted. The spectral lags are therefore determined using data from the BAT instrument on *Swift* in the same energy ranges.

5. Discussion

5.1. *INTEGRAL* GRBs of particular note

GRB 031203 is the third nearest GRB at $z = 0.1055$ (Prochaska et al. 2004) and is notable for its unambiguous association with the supernova SN 2003lw (Malesani et al.

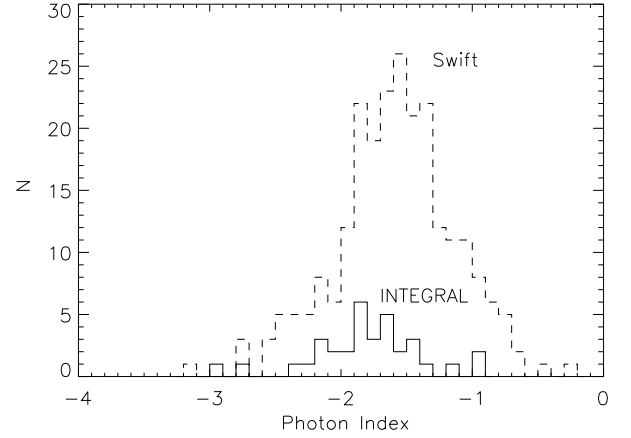


Fig. 8. Power-law photon index distribution for *INTEGRAL* GRBs detected between October 2002 and July 2007 (solid line) and *Swift* GRBs detected between November 2004 and July 2007 (dashed line), in the 20–200 keV and 15–150 keV energy bands, respectively. The *Swift* data for 238 GRBs is taken from http://swift.gsfc.nasa.gov/docs/swift/archive/grb_table.html.

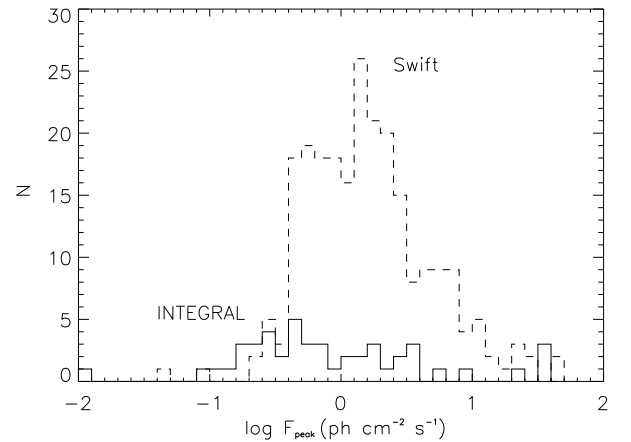


Fig. 9. Peak flux distribution for GRBs detected by *INTEGRAL* (20–200 keV, solid line) and *Swift* (15–150 keV, dashed line). The *Swift* data for 237 GRBs is taken from http://swift.gsfc.nasa.gov/docs/swift/archive/grb_table.html.

2004). It is a confirmed low-luminosity GRB with an isotropic energy of $\sim 4 \times 10^{49}$ erg (20–200 keV) (Sazonov et al. 2004) and a lag of $0.17^{+0.04}_{-0.03}$ s between 25–50 and 50–300 keV. The IBAS localisation of GRB 031203 enabled *XMM-Newton* to begin follow-up observations 6 hours later (Santos-Lleo et al. 2003). The X-ray observations showed concentric ring-like structures centred on the GRB location, making this the first detection of a GRB X-ray halo, caused by X-ray scattering from dust columns in our galaxy along the line of sight to the GRB (Vaughan et al. 2004; Tiengo & Mereghetti 2006). Dust scattering X-ray halos have recently been observed for two *Swift* GRBs (Vianello et al. 2007). The X-ray observations of GRB 031203 inferred a very high soft X-ray flux for this burst, implying that this GRB may have been an X-ray Flash (XRF) (Watson et al. 2004, 2006; Sazonov et al. 2006).

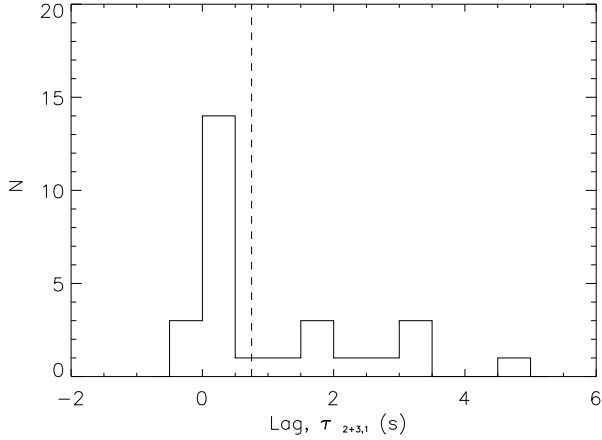


Fig. 10. Spectral lag distribution for the 28 *INTEGRAL* GRBs for which a lag could be measured between 25–50 keV and 50–300 keV ($\tau_{2+3,1}$). The distribution is separated by the dashed line into short-lag and long-lag GRBs at $\tau_{2+3,1} = 0.75$ s.

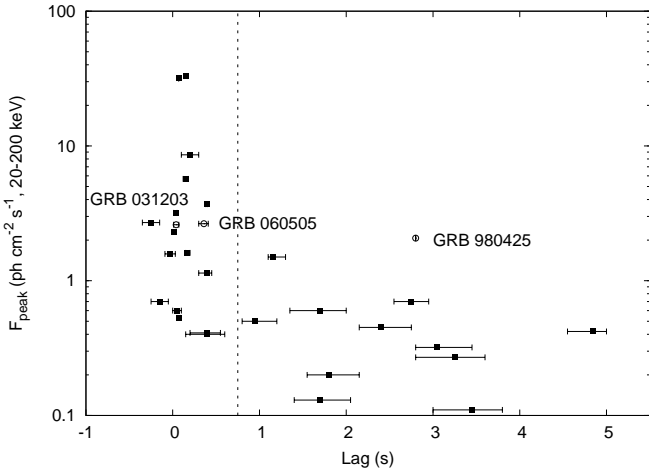


Fig. 11. Spectral lag distribution of *INTEGRAL* GRBs as a function of peak flux (20–200 keV). The SN bursts GRB 980425 and GRB 031203 are identified and represented by open circles, as is GRB 060505 which does not have an associated SN. XRF 060218 has a peak flux of $0.6 \text{ ph cm}^{-2} \text{ s}^{-1}$ and is not included in the figure because of its very long lag of 61 ± 26 s. GRBs with the longest lags tend to have low peak fluxes, whereas GRBs with short lags have both low and high peak fluxes. The dashed line indicates the separation between long and short-lag GRBs at $\tau_{2+3,1} = 0.75$ s.

GRB 041219a is the brightest burst localised by *INTEGRAL* (McBreen et al. 2006). The peak flux of $43 \text{ ph cm}^{-2} \text{ s}^{-1}$ (20 keV–8 MeV, 1 s integration) is greater than that for $\sim 98\%$ of all bursts and the total duration of ~ 520 s is longer than all but a small number of bursts. The SPI instrument was used to measure GRB polarisation through multiple scattering events in its 19 Ge detectors (Kalemci et al. 2004), since the scatter angle distribution depends on the polarisation of the incoming photons (Lei et al. 1997). A search for linear polarisation in the most intense pulse (66 seconds) in GRB 041219a and sub-intervals was performed. Kalemci et al. (2007) and McGlynn et al. (2007) have shown that there is evidence for a high degree of polarisation, but at a low significance level.

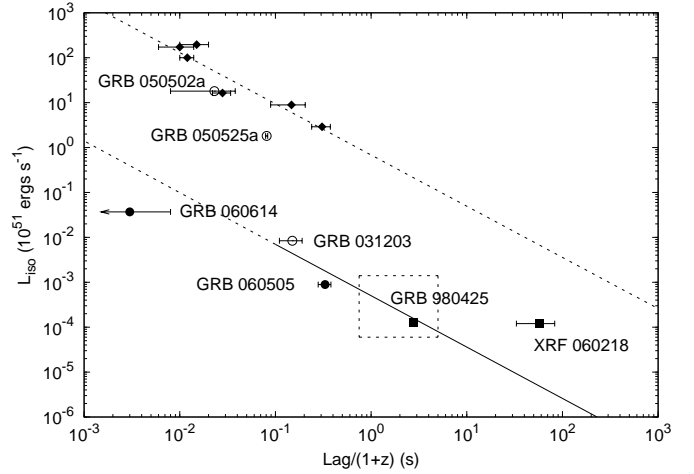


Fig. 12. Isotropic peak luminosity ($\times 10^{51} \text{ ergs s}^{-1}$, 50–300 keV) as a function of spectral lag measured between 25–50 keV and 100–300 keV. The two exceptions are GRB 060505 and GRB 060614 for which the lag was measured between 25–50 keV and 50–100 keV and 15–25 keV and 50–100 keV, respectively. The dashed line is the anti-correlation obtained for 6 bursts (diamonds) at known redshift (Norris et al. 2000). The 3 *INTEGRAL* GRBs with a redshift and measured lag are represented by open circles, including the SN burst GRB 031203. The other low-luminosity SN bursts GRB 980425 and XRF 060218 are identified and represented by squares and the two GRBs without SNe by filled circles. The long-lag GRBs lie within the dashed box if they are at the adopted distance of 250 Mpc, with peak luminosities ranging from 6×10^{46} to $1.4 \times 10^{48} \text{ ergs s}^{-1}$ and total luminosities from 10^{48} to 10^{50} ergs. The solid line is the proposed lag-luminosity relationship for the low-luminosity GRBs and extrapolates to short GRBs at low values of the lag, e.g. GRB 060614, which lies in the region of the plot occupied by short GRBs. No k-correction was applied to the data.

5.2. Afterglows of *INTEGRAL* GRBs

X-ray observations were performed for 2 long-lag GRBs with *XMM-Newton* (Gonzalez-Riestra & Rodriguez-Pascual 2004; Rodriguez-Pascual & Gonzalez-Riestra 2004) and 5 long-lag GRBs with *Swift* (Kennea et al. 2005; Mangano et al. 2005; Parola et al. 2005; Kennea et al. 2006; Vergani et al. 2007). There were also X-ray observations of 8 of the GRBs with no lag measurement. The median X-ray flux for the long-lag GRBs is $\sim 4 \times 10^{-13} \text{ erg cm}^{-2} \text{ s}^{-1}$ between 5 to 10 hours after the burst, with an upper limit in the two cases of non-detection of $\sim 4 \times 10^{-14} \text{ erg cm}^{-2} \text{ s}^{-1}$, indicating that the long-lag weak GRBs tend to have a weak X-ray afterglow component. In contrast, the other *INTEGRAL* GRBs with a measured afterglow have a typical flux of $\sim 9 \times 10^{-13} \text{ erg cm}^{-2} \text{ s}^{-1}$ between 2 and 12 hours after the burst.

Of ~ 300 GRBs localised by *Swift* up to November 2007, $\sim 60\%$ have optical or near-IR afterglows and only $\sim 30\%$ have measured redshifts (Coward et al. 2008), even though deep observations down to ~ 21 – 22 magnitudes are carried out for most events within 24 hours of the burst. Dark GRBs without a detectable afterglow may therefore make up a significant proportion of the GRB population.

Almost 70% (31/46) of the GRBs observed by *INTEGRAL* do not have a detected optical counterpart, including 9 of the 11 long-lag GRBs. The optical observations revealed faint afterglows for GRB 040323 and GRB 040827, and near-IR after-

glows for GRB 040223 and GRB 040624 (Filliatre et al. 2006). A non-spectroscopic redshift in the range $0.5 < z < 1.7$ was obtained for GRB 040827 (de Luca et al. 2005). The IBIS error box of GRB 060114 contains galaxies from the cluster A1651 ($z=0.087$) and the optical afterglow was fainter than $R = 19$ just 1.9 min after the GRB (Guidorzi et al. 2006). Only one radio afterglow has been detected for the long-lag GRBs (Frail 2005), compared to a total of 8/46 for all of the *INTEGRAL* GRBs.

GRB 040223 and GRB 040624 (Filliatre et al. 2006) provide good examples of GRBs with dark or faint optical afterglows. GRB 040223 was observed close to the galactic plane, so NIR observations were carried out to overcome the high dust obscuration. Observations were undertaken at the NTT of ESO, 17 hours after the GRB and no afterglow was found. GRB 040624 was located far from the galactic plane at high latitude where the optical extinction is negligible. Afterglow observations were carried out 13 hours after the burst using the VLT and TNG. Magnitude limits were obtained in the optical that are fainter than the very faint end of the distribution of the magnitudes of a compilation of 39 promptly observed counterparts. The position of GRB 040624 is less than $5'$ from a galaxy in the cluster A1651. A search for a supernova was carried out up to a month after the GRB but none was found to a faint limit of $R > 22.6$ (D'Avanzo et al. 2004).

The lack of a detected optical afterglow may be due to a number of factors. Possible explanations include dust obscuration, a low-density environment, an intrinsically faint afterglow in the optical, a rapidly decaying afterglow or the burst occurring at a high redshift (e.g. Jakobsson et al. 2004; Rol et al. 2005). Dust obscuration may be due to a burst environment with a high gas column density (e.g. Lamb 2001; Castro-Tirado et al. 2007) or dust in the host galaxy along the line of sight to the GRB ($\sim 10\%$ of dark events, Piro et al. (2002)). Low-density GRB environments can also produce a very faint optical afterglow but the association between GRBs and core-collapse SNe does not favour this scenario (Taylor et al. 1998). Some GRBs have intrinsically faint afterglows (Fynbo et al. 2001). GRBs at high redshift can only account for $\sim 10\%$ of these dark bursts (e.g. Gorosabel et al. 2004; Castro-Tirado et al. 2006). Using early observations of *Swift* GRBs, Roming et al. (2006) found that $\sim 25\%$ of the sample were extinguished by galactic dust, $\sim 25\%$ by absorption in the local burst environment and $\sim 30\%$ were most probably affected by Ly- α absorption at high redshift.

5.3. *INTEGRAL* Spectra

Most GRB continuum spectra can be fit by the Band model (Band et al. 1993), an empirical function comprising two smoothly broken power laws. The distributions of the low energy power-law photon index and high energy power-law photon index are distributed around values of $\alpha = -1$ and $\beta = -2.2$, respectively, for time-resolved spectra of 156 GRBs detected by BATSE (Preece et al. 2000). The majority of GRBs have low energy power-law spectral indices in the range $-2 < \alpha < 0$ (e.g. Preece et al. 2000). Of the 10 *INTEGRAL* GRBs fit by the Band model (Table 3), all have low energy spectral indices consistent with synchrotron emission, i.e. $-3/2 < \alpha < -2/3$.

A thermal component of the prompt emission spectra has been proposed by several authors (e.g. Ghirlanda et al. 2003; Kaneko et al. 2006; Ryde 2005; Bosnjak et al. 2006; McBreen et al. 2006). In a study of BATSE GRBs with very hard spectra, Ghirlanda et al. (2003) found that the time-resolved spectra were not adequately described by non-thermal emission models and that the early parts of the bursts were well fit by a

blackbody component. Ryde (2005) has shown that GRB spectra may be composed of a thermal and a power-law component. McBreen et al. (2006) found that for quasithermal model fits to the precursor and main emission of the *INTEGRAL* burst GRB 041219a, the blackbody component is more dominant in the precursor of the burst, while the main burst emission is well fit by both the Band and quasithermal models. The blackbody temperature decreases from the precursor of GRB 041219a to the main burst emission as expected from Ryde (2005). The 10 bright GRBs in Table 3 are equally well fit by the Band model and blackbody + power-law model fits to the average prompt emission spectra, with similar χ^2 values.

Many of the *INTEGRAL* GRBs in Table 6 have steep power-law spectra, which are significantly outside the usual range of the Band model low-energy spectral index of $-3/2 < \alpha < -2/3$. For these GRBs, the power-law index is similar to the high energy photon index above the break energy, with typical values of β between -2 and -2.5 (Preece et al. 2000). If the steep power-law indices are assumed to be β , the break energy, E_0 , must be at or below the sensitivity threshold of IBIS, ~ 20 keV. There is therefore an excess of counts in the X-ray/soft γ -ray region, implying that they are X-ray rich. The peak energy is given by $E_{peak} = (2 + \alpha)E_0$ and has a value of $E_{peak} = E_0/2$ for a typical value of $\alpha = -1.5$. These GRBs have a low E_{peak} and will have a low luminosity if they are at low redshift (Amati et al. 2007).

INTEGRAL has detected a number of X-ray rich GRBs. X-ray flashes, X-ray rich GRBs and classical GRBs appear to possess a continuum of spectral properties and it is probable that they have a similar origin (Sakamoto et al. 2005). *INTEGRAL* X-ray rich bursts tend to be weak and their time profiles consist of long, slow pulses (see Appendix). Examples include GRB 040223 (Fig. A.1 (i)), GRB 040624 (Fig. A.2 (a)), GRB 050626 (Fig. A.3 (d)) and GRB 060130 (Fig. A.3 (k)).

5.4. The rate of *INTEGRAL* GRBs

GRBs detected at off-axis angles outside the FCFoV of IBIS have a higher peak flux (Fig. 4) because of the reduction in collecting area. For this reason, we estimate the rate of GRBs both in the FCFoV and in the PCFoV at greater than 50% coding. There are 11 GRBs within the FCFoV of 0.025 sr of IBIS in 4 years of observation time, yielding an all-sky rate of ~ 1400 yr $^{-1}$ above the threshold of ~ 0.15 ph cm $^{-2}$ s $^{-1}$ in the energy range 20–200 keV. The 4 long-lag GRBs in the FCFoV give a rate of ~ 500 yr $^{-1}$. The 33 GRBs within the PCFoV to the 50% coding level yield an all-sky rate of ~ 930 yr $^{-1}$ and ~ 230 yr $^{-1}$ for the 8 long-lag GRBs above the higher threshold of ~ 0.25 ph cm $^{-2}$ s $^{-1}$. The long-lag GRBs contribute significantly at faint flux levels and appear to form a separate population in the log N-log P distribution (Fig. 5). The rate of GRBs is in good agreement with the values obtained from the more sensitive analysis of BATSE archival data (Kommers et al. 2001; Stern et al. 2001).

5.5. The population of long-lag GRBs with low luminosity

The lack of redshift determinations for the weak GRBs detected by IBIS prohibits progress by using individual GRBs. However there are a number of redshift indicators that can be used on weak GRBs. In this case the best redshift indicator is the spectral lag which combines the spectral and temporal properties of the prompt GRB emission. GRBs have a long lag when a typical value of 0.1 s is redshifted by a large factor or alternatively is an intrinsic property of a low-luminosity GRB such as

GRB 980425 and XRF 060218. The rate of $z > 5$ GRBs in IBIS has been modelled (Salvaterra et al. 2008; Gorosabel et al. 2004; Guetta & Piran 2007; Lapi et al. 2008) and is unlikely to be more than 1 or 2 GRBs in 5 years of observations. The long lag is therefore taken to be an intrinsic property of most of the long-lag GRBs indicating their low luminosity and we investigate the consequences.

The median properties of long and short lag *INTEGRAL* GRBs are given in Table 6 for the 28 bursts with a measured value of $\tau_{2+3,1}$. Approximately 40% of *INTEGRAL* GRBs with a measured lag belong to the long-lag category. The median peak flux for long-lag GRBs is a factor of ~ 5 lower than for GRBs with short lags.

The distribution of the *INTEGRAL* GRBs in supergalactic coordinates is shown in Fig. 13. All of the *INTEGRAL* GRBs are divided almost equally between the half of the sky above and below $\pm 30^\circ$, in agreement with the exposure map which has $\sim 52\%$ of the exposure time within $\pm 30^\circ$ of the supergalactic plane. However, 10 of the 11 long-lag GRBs are concentrated at supergalactic latitudes between $\pm 30^\circ$. The quadrupole moment (Hartmann et al. 1996) has a value of $Q = 0.007 \pm 0.043$ for all *INTEGRAL* GRBs and $Q = -0.225 \pm 0.090$ for the long-lag GRBs. The quadrupole moment of the 47 bursts is consistent with zero and an isotropic distribution. The non-zero moment of the long-lag bursts indicates an anisotropy in the distribution of these GRBs with respect to the supergalactic plane. The binomial probability that this is a chance occurrence is 7×10^{-3} . GRB 980425 and XRF 060218 have long lags and lie within $\pm 30^\circ$ of the supergalactic plane, while GRB 031203 has a relatively short lag and lies at a high supergalactic latitude. The long-lag GRBs observed with BATSE are also significantly concentrated in the direction $\pm 30^\circ$ of the supergalactic plane with a quadrupole moment $Q = -0.097 \pm 0.038$ (Norris 2002). The combined results of more than 14 years of observations with IBIS and BATSE lead us to conclude that long-lag GRBs trace the features of the nearby large-scale structure of the Universe as revealed with superclusters, galaxy surveys (Lahav et al. 2000; Stoughton et al. 2002) and the very high energy cosmic rays (Abraham et al. 2007). This result is a further indication that most long-lag GRBs are nearby and have low luminosity. The local supercluster seems to be appended to a web of filaments and sheets, rather than an isolated pancake structure, with superclusters evident to ~ 400 Mpc. It has been pointed out that weak BATSE GRBs appear to be correlated with galaxies out to distances of ~ 155 Mpc with the limit determined by galaxy surveys (Chapman et al. 2007).

A nearby population of long-lag, low-luminosity GRBs has previously been proposed based on the detections of GRB 980425, GRB 031203 and XRF 060218 (e.g. Guetta et al. 2004; Daigne & Mochkovitch 2007). GRB 980425 has an isotropic-equivalent γ -ray energy release of $\sim 10^{48}$ ergs, approximately 3 orders of magnitude lower than that of “standard” GRBs, assuming its association with SN 1998bw (Galama et al. 1998) and redshift of $z = 0.0085$ (Tinney et al. 1998). XRF 060218, the second closest GRB localised to date, was detected at a redshift of $z = 0.033$ (Mirabal et al. 2006). This burst had an extremely long duration ($T_{90} \sim 2100$ s), a very low isotropic energy of $\sim 6 \times 10^{49}$ ergs and is classified as an XRF (Campana et al. 2006). The distance to the long-lag GRBs can also be constrained by association and comparison with the two low luminosity bursts GRB 980425 ($\tau \sim 2.8$ s) and XRF 060218 ($\tau \sim 60$ s). The distances to GRB 980425 (Galama et al. 1998) and XRF 060218 (Soderberg et al. 2006) are 36 Mpc and 145 Mpc,

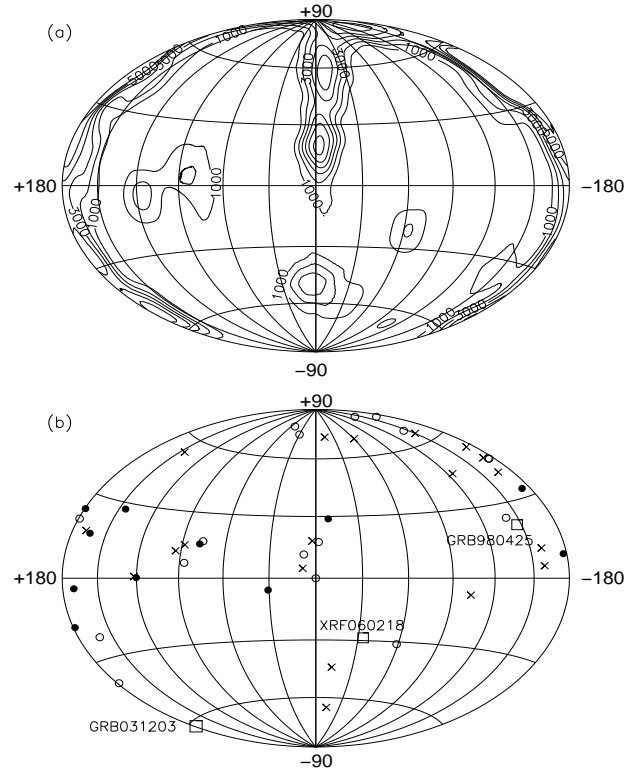


Fig. 13. (a) *INTEGRAL* exposure map in supergalactic coordinates up to July 2007 (contours in units of kiloseconds). (b) The distribution of *INTEGRAL* GRBs in supergalactic coordinates; the open circles represent short-lag GRBs ($\tau_{2+3,1} < 0.75$ s) and filled-in circles those GRBs with long lags ($\tau_{2+3,1} > 0.75$ s). The 16 GRBs for which a lag could not be determined are denoted by an ‘x’, as are the XRFs which do not have a measured lag between 25–50 keV and 50–300 keV, and the short burst GRB 070707. Ten out of the 11 long-lag GRBs are within $\pm 30^\circ$ of the supergalactic plane.

respectively, and these bursts would have been detected in the FCFoV of IBIS to 135 Mpc and 290 Mpc. The association of the long-lag GRBs with the known low luminosity GRBs and with the supergalactic plane implies that they are at similar distances. GRB 060505 has no SN to faint limits and has a smaller lag of ~ 0.4 s and a distance of 404 Mpc (Fynbo et al. 2006; McBreen et al. 2008).

The region marked with a box on the lag-luminosity plot (Fig. 12) contains the long-lag GRBs if they belong to the low luminosity population at an adopted distance of 250 Mpc. The box contains the prototype low luminosity GRB 980425 and is bracketed on one side by GRB 060218 and on the other by GRB 060505 ($\tau \sim 0.4$ s) and GRB 031203 ($\tau \sim 0.17$ s) and at short lag by GRB 060614 which lies in the region occupied by short GRBs (Gehrels et al. 2006). With a long lag of ~ 2.8 s, GRB 980425 qualitatively follows the lag-luminosity trend but falls significantly below the relation in Fig. 12 (Norris 2002), as do GRB 031203 (Sazonov et al. 2004) and GRB 060218 (Liang et al. 2006). The solid line in Fig. 12 is the proposed lag-luminosity relationship for low-luminosity GRBs and is parallel to but shifted from the corresponding fit for the long cosmological GRBs by a factor of $\sim 10^3$.

Both GRB 980425 and GRB 031203 violate the Amati correlation (Amati et al. 2007) between isotropic energy, E_{iso} , and peak energy, E_{peak} (Ghisellini et al. 2006). GRB 060218 how-

ever is consistent with the the Amati relation, fuelling the debate that GRB 980425 and GRB 031203 may just be apparent outliers and their intrinsic properties may be consistent with the relations. Invoking a jet geometry, the low observed luminosities for these GRBs may be due to such factors as wider jet opening angle, variations in viewing angle such that the more off-axis a burst is viewed the lower its luminosity or profiled jets with the Lorentz factor decreasing off-axis (Yamazaki et al. 2003; Ramirez-Ruiz et al. 2005).

It has also been proposed that GRBs 980425 and 031203 are intrinsically sub-energetic events seen on-axis, based on afterglow observations (Soderberg et al. 2004) and within the constraints of the internal shock model (Daigne & Mochkovitch 2007). Such inherently sub-luminous events would be permitted by the internal shock model, where the burst is produced by a mildly relativistic outflow. If intrinsically low-luminosity, the rate of bursts such as GRB 980425 may be far higher than that of “standard” cosmological GRBs but only detectable locally.

The possibility that low luminosity GRBs could be part of the same population as cosmological GRBs or form a separate sub-energetic population with a much higher rate has been considered (Soderberg et al. 2006; Cobb et al. 2006; Chapman et al. 2007; Guetta & Della Valle 2007; Liang et al. 2007; Coward et al. 2008; Le & Dermer 2007; Virgili et al. 2008). The large number of long-lag GRBs detected with IBIS favours the latter conclusion and indicates that low redshift GRBs are dominated by the low luminosity class.

The collapsar model can account for low-luminosity GRBs if they have low Lorentz factors and fail to produce highly-relativistic jets due to baryon loading (Woosley & MacFadyen 1999). It has also been proposed that the nature of the central engine may be different, e.g., a magnetar progenitor as opposed to a black hole (e.g. Soderberg et al. 2006; Toma et al. 2007). Some authors suggest that the γ -rays are produced in a supernova shock breakout (e.g. Matzner & McKee 1999; Ghisellini et al. 2007). A very luminous X-ray outburst was observed from the core collapse SN in NGC 2770 (Soderberg et al. 2008) that may be the shock breakout as recently observed from a red supergiant in a galaxy in the COSMOS field (Schawinski et al. 2008) or an X-ray flash (Xu et al. 2008; Li 2008).

We evaluate the rate of GRBs over the whole sky using the 8 long-lag GRBs in the PCFoV (Table 6) at 50% coding (0.1 sr) over an exposure time of 4 years, adopting a distance of 250 Mpc and assuming that 2 of the 8 GRBs are not at low redshift. We obtain $2640 \text{ Gpc}^{-3} \text{ yr}^{-1}$ which is $\sim 25\%$ of the local rate of Type Ib/c SNe (Soderberg et al. 2006). The major uncertainty in this estimate is the distance, where a change of only a factor of 2 increases or decreases this number by 8 to 21, $100 \text{ Gpc}^{-3} \text{ yr}^{-1}$ and $330 \text{ Gpc}^{-3} \text{ yr}^{-1}$, respectively.

The rate of low-luminosity GRBs at the adopted distance of 250 Mpc exceeds the upper limit of 3% or $< 300 \text{ Gpc}^{-3} \text{ yr}^{-1}$ of Type Ib/c SN producing GRBs, which was derived assuming that all low luminosity GRBs would produce a SN and be as radio bright as the SN GRBs (Soderberg et al. 2006). However, the low luminosity GRB 060605 has no associated SN to faint limits and is evidence for a quiet end for some massive stars (Fynbo et al. 2006; Dado et al. 2006; McBreen et al. 2008). A GRB may occur without a corresponding SN being observed if the ^{56}Ni does not have sufficient energy to escape the black hole or if the progenitor star has a low angular momentum. The association of low luminosity GRBs with the supergalactic plane is not proof that they are associated with clusters of galaxies but indicates that clusters may play a role. It is interesting to note that the rate of Type Ia SNe is higher in elliptical galaxies in clus-

ters than in field ellipticals by a factor of ~ 3 (Mannucci et al. 2008). This effect is due to galaxy-galaxy interactions in clusters (Boselli & Gavazzi 2006) either producing a small amount of young stars or affecting the evolution and properties of binary systems. In the latter case, there should also be an increase in the merger rate of white dwarfs or a white dwarf with a neutron star or black hole. A merger involving a white dwarf (Fryer et al. 1999; Middleditch 2004; Levan et al. 2006; King et al. 2007) should produce a long GRB that is likely to be fainter than the formation of a black hole in cosmological GRBs. There will be no supernova in the merger of a white dwarf with a neutron star or black hole, and probably a faint afterglow. In addition, the merger could take place in the intercluster region without a host galaxy if the binary is ripped from its host in the merger interaction involving the cluster galaxies (Niino & Totani 2008).

6. Conclusions

INTEGRAL observations of gamma-ray bursts have yielded many interesting results and offer significant insight into the prompt γ -ray emission. IBAS successfully provides accurate, fast localisations of GRBs to the community at a rate of ~ 0.8 GRBs per month, enabling multi-wavelength afterglow observations to be carried out by other space-based missions and ground-based telescopes.

We have presented the spectral, spatial, and temporal lag analysis of the 47 *INTEGRAL* GRBs up to July 2007. Most weak *INTEGRAL* GRBs are well fit with a power law, while bright GRBs can be fit by both the Band and quasithermal models. Approximately 40% of the GRBs for which a lag was measured have long spectral lags (> 0.75 s between 25–50 and 50–300 keV). The long-lag GRBs are characterised by low peak flux, long slow pulses and are concentrated towards the supergalactic plane, reflecting the nearby large-scale structure of the Universe.

INTEGRAL therefore detects a large proportion of faint, long-lag GRBs that are inferred to be local. The sensitivity of IBIS is such that it can detect very faint GRBs, allowing *INTEGRAL* to probe the population of low-luminosity GRBs with long lags. This population appears to be distinct from that of high-luminosity GRBs and dominates the local GRB population.

Acknowledgements. The authors thank Darach Watson and Rob Preece for useful discussions and comments, Andreas von Kienlin for providing the GRB 060901 data and Erik Kuulkers for the *INTEGRAL* exposure map data. SMB acknowledges the support of the European Union through a Marie Curie Intra-European Fellowship within the Sixth Framework Program.

References

- Abraham, J., Abreu, P., Aglietta, M., et al. 2007, *Science*, 318, 938
- Amati, L., Della Valle, M., Frontera, F., et al. 2007, *A&A*, 463, 913
- Band, D., Matteson, J., Ford, L., et al. 1993, *ApJ*, 413, 281
- Band, D. L. 1997, *ApJ*, 486, 928
- Beckmann, V., Borkowski, J., Courvoisier, T. J.-L., et al. 2003, *A&A*, 411, L327
- Boella, G., Butler, R. C., Perola, G. C., et al. 1997, *A&AS*, 122, 299
- Bolmont, J., Atteia, J. L., Jacholkowska, A., Piron, F., & Pizzichini, G. 2006, *astro-ph/0603725*
- Boselli, A. & Gavazzi, G. 2006, *PASP*, 118, 517
- Bosnjak, Z., Celotti, A., Ghirlanda, G., Della Valle, M., & Pian, E. 2006, *A&A*, 447, 121
- Butler, N. R., Kocevski, D., & Bloom, J. S. 2008, *astro-ph/0802.3396*
- Campana, S., Mangano, V., Blustin, A. J., et al. 2006, *Nature*, 442, 1008
- Castro-Tirado, A. J., Bremer, M., McBreen, S., et al. 2007, *A&A*, 475, 101
- Castro-Tirado, A. J., Jelínek, M., Pandey, S. B., et al. 2006, *A&A*, 459, 763
- Chapman, R., Tanvir, N. R., Priddey, R. S., & Levan, A. J. 2007, *MNRAS*, 382, L21

- Chen, L., Lou, Y.-Q., Wu, M., et al. 2005, *ApJ*, 619, 983
- Cheng, L. X., Ma, Y. Q., Cheng, K. S., Lu, T., & Zhou, Y. Y. 1995, *A&A*, 300, 746
- Cobb, B. E., Bailyn, C. D., van Dokkum, P. G., & Natarajan, P. 2006, *ApJ*, 645, L113
- Coward, D. M., Guetta, D., Burman, R. R., & Imerito, A. 2008, *MNRAS*, 386, 111
- Dado, S., Dar, A., De Rujula, A., & Plaga, R. 2006, *astro-ph/0611161*
- Daigne, F. & Mochkovitch, R. 2003, *MNRAS*, 342, 587
- Daigne, F. & Mochkovitch, R. 2007, *A&A*, 465, 1
- D'Avanzo, P., Fugazza, D., Melandri, A., et al. 2004, *GCN* 2632
- D'Avanzo, P., Malesani, D., Campana, S., et al. 2006, *astro-ph/0612644*
- de Luca, A., Melandri, A., Caraveo, P. A., et al. 2005, *A&A*, 440, 85
- Donaghy, T. Q., Lamb, D. Q., Sakamoto, T., et al. 2006, *astro-ph/0605570*
- Fenimore, E., Barthelmy, S., Cummings, J., et al. 2004, *GCN*, 2905
- Filliatre, P., Covino, S., D'Avanzo, P., et al. 2006, *A&A*, 448, 971
- Filliatre, P., D'Avanzo, P., Covino, S., et al. 2005, *A&A*, 438, 793
- Fishman, G. J. & Meegan, C. A. 1995, *ARA&A*, 33, 415
- Foley, R. J., Chen, H.-W., Bloom, J. S., & Prochaska, J. X. 2005, *GCN* 3483
- Frail, D. A. 2005, *GCN* 4350
- Fryer, C. L., Woosley, S. E., Herant, M., & Davies, M. B. 1999, *ApJ*, 520, 650
- Fynbo, J. P. U., Watson, D., Thöne, C. C., et al. 2006, *Nature*, 444, 1047
- Fynbo, J. U., Jensen, B. L., Gorosabel, J., et al. 2001, *A&A*, 369, 373
- Galama, T. J., Vreeswijk, P. M., van Paradijs, J., et al. 1998, *Nature*, 395, 670
- Gehrels, N., Chincarini, G., Giommi, P., et al. 2004, *ApJ*, 611, 1005
- Gehrels, N., Norris, J. P., Barthelmy, S. D., et al. 2006, *Nature*, 444, 1044
- Ghirlanda, G., Celotti, A., & Ghisellini, G. 2003, *A&A*, 406, 879
- Ghisellini, G., Ghirlanda, G., Mereghetti, S., et al. 2006, *MNRAS*, 372, 1699
- Ghisellini, G., Ghirlanda, G., & Tavecchio, F. 2007, *MNRAS*, 382, L77
- Gonzalez-Riestra, R. & Rodriguez-Pascual, P. 2004, *GCN* 2533
- Gorosabel, J., Lund, N., Brandt, S., Westergaard, N. J., & Castro Cerón, J. M. 2004, *A&A*, 427, 87
- Götz, D., Mereghetti, S., Hurlley, K., et al. 2003, *A&A*, 409, 831
- Gotz, D., Mereghetti, S., Paizis, A., et al. 2006, *GCN*, 5665
- Grebenev, S. A. & Chelovekov, I. V. 2007, *Astronomy Letters*, 33, 789
- Guetta, D. & Della Valle, M. 2007, *ApJ*, 657, L73
- Guetta, D., Perna, R., Stella, L., & Vietri, M. 2004, *ApJ*, 615, L73
- Guetta, D. & Piran, T. 2007, *Journal of Cosmology and Astro-Particle Physics*, 7, 3
- Guidorzi, C., Gomboc, A., Mundell, C. G., et al. 2006, *GCN* 4504
- Gupta, V., Das Gupta, P., & Bhat, P. N. 2002, *astro-ph/0206402*
- Hafizi, M. & Mochkovitch, R. 2007, *A&A*, 465, 67
- Hakkila, J. & Giblin, T. W. 2004, *ApJ*, 610, 361
- Hakkila, J., Giblin, T. W., Norris, J. P., Fragile, P. C., & Bonnell, J. T. 2008, *ApJ*, 677, L81
- Hakkila, J., Giblin, T. W., Young, K. C., et al. 2007, *ApJS*, 169, 62
- Hartmann, D. H., Briggs, M. S., & Mannheim, K. 1996, in *American Institute of Physics Conference Series*, Vol. 384, 397
- Hurlley, K., Mitrofanov, I., Kozlyev, A., et al. 2006, *ApJS*, 164, 124
- Ioka, K. & Nakamura, T. 2001, *ApJ*, 554, L163
- Jakobsson, P., Hjorth, J., Fynbo, J. P. U., et al. 2004, *ApJ*, 617, L21
- Kalemci, E., Boggs, S., Wunderer, C., & Jean, P. 2004, in *5th INTEGRAL Workshop on the INTEGRAL Universe*, 859
- Kalemci, E., Boggs, S. E., Kouveliotou, C., Finger, M., & Baring, M. G. 2007, *ApJS*, 169, 75
- Kaneko, Y., Preece, R. D., Briggs, M. S., et al. 2006, *ApJS*, 166, 298
- Kennea, J. A., Burrows, D. N., Zhang, B., & Gehrels, N. 2005, *GCN* 3426
- Kennea, J. A., Godet, O., Burrows, D. N., & Gehrels, N. 2006, *GCN* 4624
- King, A., Olsson, E., & Davies, M. B. 2007, *MNRAS*, 374, L34
- Kocevski, D. & Liang, E. 2003, *ApJ*, 594, 385
- Kommers, J. M., Lewin, W. H. G., Kouveliotou, C., et al. 2001, *VizieR Online Data Catalog*, 213, 40385
- Kouveliotou, C., Meegan, C. A., Fishman, G. J., et al. 1993, *ApJ*, 413, L101
- Labanti, C., Di Cocco, G., Ferro, G., et al. 2003, *A&A*, 411, L149
- Lahav, O., Santiago, B. X., Webster, A. M., et al. 2000, *MNRAS*, 312, 166
- Lamb, D. Q. 2001, in *Gamma-ray Bursts in the Afterglow Era*, ed. E. Costa, F. Frontera, & J. Hjorth, 297
- Lapi, A., Kawakatu, N., Bosnjak, Z., et al. 2008, *astro-ph/0802.0787*
- Le, T. & Dermer, C. D. 2007, *ApJ*, 661, 394
- Lebrun, F., Leray, J. P., Lavocat, P., et al. 2003, *A&A*, 411, L141
- Lei, F., Dean, A. J., & Hills, G. L. 1997, *Space Science Reviews*, 82, 309
- Levan, A. J., Wynn, G. A., Chapman, R., et al. 2006, *MNRAS*, 368, L1
- Li, L.-X. 2008, *astro-ph/0803.0079*
- Liang, E., Zhang, B., Virgili, F., & Dai, Z. G. 2007, *ApJ*, 662, 1111
- Liang, E.-W., Zhang, B.-B., Stamatikos, M., et al. 2006, *ApJ*, 653, L81
- Lloyd-Ronning, N. M. & Petrosian, V. 2002, *ApJ*, 565, 182
- Lund, N., Budtz-Jørgensen, C., Westergaard, N. J., et al. 2003, *A&A*, 411, L231
- Malaguti, G., Bazzano, A., Beckmann, V., et al. 2003, *A&A*, 411, L307
- Malesani, D., Tagliaferri, G., Chincarini, G., et al. 2004, *ApJ*, 609, L5
- Mangano, V., Mineo, T., Parola, V. L., et al. 2005, *GCN* 3564
- Mannucci, F., Maoz, D., Sharon, K., et al. 2008, *MNRAS*, 383, 1121
- Marcinkowski, R., Denis, M., Bulik, T., et al. 2006, *A&A*, 452, 113
- Mas-Hesse, J. M., Giménez, A., Culhane, J. L., et al. 2003, *A&A*, 411, L261
- Matzner, C. D. & McKee, C. F. 1999, *ApJ*, 510, 379
- McBreen, S., Foley, S., Watson, D., et al. 2008, *ApJ*, 677, L85
- McBreen, S., Hanlon, L., McGlynn, S., et al. 2006, *A&A*, 455, 433
- McBreen, S., Quilligan, F., McBreen, B., Hanlon, L., & Watson, D. 2001, *A&A*, 380, L31
- McGlynn, S., Clark, D. J., Dean, A. J., et al. 2007, *A&A*, 466, 895
- McGlynn, S., Foley, S., McBreen, S., et al. 2008a, *A&A*, submitted
- McGlynn, S., McBreen, S., Hanlon, L., et al. 2005, *Nuovo Cimento C*, 28, 481
- McGlynn, S. et al. 2008b, in prep.
- Mereghetti, S., Götz, D., Andersen, M. I., et al. 2005, *A&A*, 433, 113
- Mereghetti, S., Götz, D., Beckmann, V., et al. 2003a, *A&A*, 411, L311
- Mereghetti, S., Götz, D., Borkowski, J., Walter, R., & Pedersen, H. 2003b, *A&A*, 411, L291
- Mereghetti, S., Götz, D., Tiengo, A., et al. 2003c, *ApJ*, 590, L73
- Mereghetti, S., Paizis, A., Götz, D., & Kreykenbohm, I. 2007, *GCN* 6189
- Mészáros, P. 2006, *Reports on Progress in Physics*, 69, 2259
- Middleditch, J. 2004, *ApJ*, 601, L167
- Mirabal, N., Halpern, J. P., An, D., Thorstensen, J. R., & Terndrup, D. M. 2006, *ApJ*, 643, L99
- Moran, L., Mereghetti, S., Götz, D., et al. 2005, *A&A*, 432, 467
- Niino, Y. & Totani, T. 2008, *ApJ*, 677, L23
- Norris, J., Barthelmy, S., Gehrels, N., et al. 2005, *GCN*, 3484
- Norris, J. P. 2002, *ApJ*, 579, 386
- Norris, J. P. & Bonnell, J. T. 2006, *ApJ*, 643, 266
- Norris, J. P., Marani, G. F., & Bonnell, J. T. 2000, *ApJ*, 534, 248
- Parola, V. L., Mangano, V., Cusumano, G., et al. 2005, *GCN* 4347
- Pellizza, L. J., Duc, P.-A., Le Floch, E., et al. 2006, *A&A*, 459, L5
- Piran, T. 2005, *Reviews of Modern Physics*, 76, 1143
- Piro, L., Frail, D. A., Gorosabel, J., et al. 2002, *ApJ*, 577, 680
- Preece, R. D., Briggs, M. S., Mallozzi, R. S., et al. 2000, *ApJS*, 126, 19
- Prochaska, J. X., Bloom, J. S., Chen, H.-W., et al. 2004, *ApJ*, 611, 200
- Prochaska, J. X., Ellison, S., Foley, R. J., & Bloom, J. S. 2005, *GCN* 3332
- Quilligan, F., McBreen, B., Hanlon, L., et al. 2002, *A&A*, 385, 377
- Ramirez-Ruiz, E., Granot, J., Kouveliotou, C., et al. 2005, *ApJ*, 625, L91
- Rau, A., Kienlin, A. V., Hurlley, K., & Lichti, G. G. 2005, *A&A*, 438, 1175
- Rees, M. J. & Mészáros, P. 2005, *ApJ*, 628, 847
- Rodriguez-Pascual, P. & Gonzalez-Riestra, R. 2004, *GCN* 2688
- Rol, E., Wijers, R. A. M. J., Kouveliotou, C., Kaper, L., & Kaneko, Y. 2005, *ApJ*, 624, 868
- Roming, P. W. A., Schady, P., Fox, D. B., et al. 2006, *ApJ*, 652, 1416
- Ryde, F. 2005, *ApJ*, 625, L95
- Ryde, F., Björnsson, C.-I., Kaneko, Y., et al. 2006, *ApJ*, 652, 1400
- Ryde, F., Kocevski, D., Bagoly, Z., Ryde, N., & Mészáros, A. 2005, *A&A*, 432, 105
- Sakamoto, T., Lamb, D. Q., Kawai, N., et al. 2005, *ApJ*, 629, 311
- Salmonson, J. D. 2000, *ApJ*, 544, L115
- Salmonson, J. D. & Galama, T. J. 2002, *ApJ*, 569, 682
- Salvaterra, R., Campana, S., Chincarini, G., Covino, S., & Tagliaferri, G. 2008, *MNRAS*, 385, 189
- Santos-Lleo, M., Calderon, P., & Gotz, D. 2003, *GCN* 2464
- Sazonov, S. Y., Lutovinov, A. A., Churazov, E. M., & Sunyaev, R. A. 2006, *Astronomy Letters*, 32, 297
- Sazonov, S. Y., Lutovinov, A. A., & Sunyaev, R. A. 2004, *Nature*, 430, 646
- Schaefer, B. E. 2004, *ApJ*, 602, 306
- Schaefer, B. E. 2007, *ApJ*, 660, 16
- Schawinski, K., Justham, S., Wolf, C., et al. 2008, *astro-ph/0803.3596*
- Shrader, C. R. 2006, in *Gamma-Ray Bursts in the Swift Era*, ed. S. S. Holt, N. Gehrels, & J. A. Nousek, Vol. 836, 185
- Soderberg, A. M., Berger, E., Page, K., et al. 2008, *astro-ph/0802.1712*
- Soderberg, A. M., Kulkarni, S. R., Berger, E., et al. 2004, *Nature*, 430, 648
- Soderberg, A. M., Kulkarni, S. R., Nakar, E., et al. 2006, *Nature*, 442, 1014
- Stern, B. E., Tikhomirova, Y., Kompaneets, D., Svensson, R., & Poutanen, J. 2001, *ApJ*, 563, 80
- Stoughton, C., Lupton, R. H., Bernardi, M., et al. 2002, *AJ*, 123, 485
- Taylor, G. B., Frail, D. A., Kulkarni, S. R., et al. 1998, *ApJ*, 502, L115
- Tiengo, A. & Mereghetti, S. 2006, *A&A*, 449, 203
- Tinney, C., Stathakis, R., Cannon, R., et al. 1998, *IAU Circ.*, 6896
- Toma, K., Ioka, K., Sakamoto, T., & Nakamura, T. 2007, *ApJ*, 659, 1420
- Ubertini, P., Lebrun, F., Di Cocco, G., et al. 2003, *A&A*, 411, L131
- Vaughan, S., Willingale, R., O'Brien, P. T., et al. 2004, *ApJ*, 603, L5
- Vedrenne, G., Roques, J.-P., Schönfelder, V., et al. 2003, *A&A*, 411, L63
- Vergani, S. D., Romano, P., & Guidorzi, C. 2007, *GCN* 6369
- Vianello, G., Tiengo, A., & Mereghetti, S. 2007, *A&A*, 473, 423

- Virgili, F., Liang, E., & Zhang, B. 2008, *astro-ph/0801.4751*
- von Kienlin, A., Beckmann, V., Covino, S., et al. 2003a, *A&A*, 411, L321
- von Kienlin, A., Beckmann, V., Rau, A., et al. 2003b, *A&A*, 411, L299
- Watson, D., Hjorth, J., Levan, A., et al. 2004, *ApJ*, 605, L101
- Watson, D., Vaughan, S. A., Willingale, R., et al. 2006, *ApJ*, 636, 967
- Winkler, C., Courvoisier, T. J.-L., Di Cocco, G., et al. 2003, *A&A*, 411, L1
- Woosley, S. E. & MacFadyen, A. I. 1999, *A&AS*, 138, 499
- Wu, B. & Fenimore, E. 2000, *ApJ*, 535, L29
- Xu, D., Zou, Y.-C., & Fan, Y.-Z. 2008, *astro-ph/0801.4325*
- Yamazaki, R., Yonetoku, D., & Nakamura, T. 2003, *ApJ*, 594, L79
- Yi, T., Liang, E., Qin, Y., & Lu, R. 2006, *MNRAS*, 367, 1751
- Zhang, B. & Mészáros, P. 2004, *International Journal of Modern Physics A*, 19, 2385
- Zhang, Z., Xie, G. Z., Deng, J. G., & Jin, W. 2006a, *MNRAS*, 373, 729
- Zhang, Z.-B., Deng, J.-G., Lu, R.-J., & Gao, H.-F. 2006b, *Chinese Journal of Astronomy and Astrophysics*, 6, 312

Table 2. GRBs detected by *INTEGRAL*. The columns refer to (from left to right): GRB; right ascension; declination; T_{90} duration; peak flux; fluence; photon index; $\chi^2/\text{degrees of freedom (d.o.f.)}$; afterglow detections in radio, R, infrared, IR, optical, O and X-ray, X. Peak fluxes, fluences and photon indices are given in the 20–200 keV energy range.

GRB	RA	DEC	T_{90} s	Peak Flux		Fluence erg cm^{-2}	Photon Index	χ^2 / d.o.f.	Afterglow
				$\text{ph cm}^{-2} \text{s}^{-1}$	$\text{erg cm}^{-2} \text{s}^{-1}$				
GRB 021125 ^a	19:47:57	28:23:35	24	22	—	$4.8 \times 10^{-5*}$	-2.2	—	—
GRB 021219 ^b	18:50:27	31:57:17	5.5	3.7	3.5×10^{-7}	9.0×10^{-7}	-2.00 ± 0.10	—	R
GRB 030131 ^c	13:28:21	30:40:43	124	1.9	1.7×10^{-7}	7.0×10^{-6}	Table 3	—	O
GRB 030227 ^d	04:57:34	20:28:16	33	1.1	9.6×10^{-8}	7.5×10^{-7}	-1.85 ± 0.20	—	X,O
GRB 030320 ^e	17:51:36	-25:18:52	48	5.7	5.4×10^{-7}	1.1×10^{-5}	-1.69 ± 0.08	—	—
GRB 030501 ^f	19:05:33	06:15:57	40	2.7	2.5×10^{-7}	3.0×10^{-6}	-1.75 ± 0.10	—	—
GRB 030529	09:40:30	-56:20:31	20	0.4	3.7×10^{-8}	4.0×10^{-7}	-2.07 ± 0.30	2.9/5	—
GRB 031203 ^{g*}	08:02:32	-39:50:47	39	2.6	2.5×10^{-7}	2.0×10^{-6}	-1.63 ± 0.06	—	X,O,R
GRB 040106 ^h	11:52:18	-46:47:15	47	0.6	6.5×10^{-8}	8.2×10^{-7}	-1.72 ± 0.15	—	X,O,R
GRB 040223 ⁱ	16:39:31	-41:55:47	258	0.2	1.6×10^{-8}	4.4×10^{-7}	-2.30 ± 0.19	20.1/20	X
GRB 040323	13:53:49	-52:20:45	14	1.5	2.0×10^{-7}	3.0×10^{-6}	-1.44 ± 0.18	10.6/8	O
GRB 040403 ^j	07:40:54	68:12:55	21	0.5	4.3×10^{-8}	5.0×10^{-7}	-1.90 ± 0.15	—	—
GRB 040422 ^k	18:42:01	01:59:04	4	2.3	1.8×10^{-7}	3.4×10^{-7}	Table 3	—	IR
GRB 040624 ^l	13:00:08	-03:34:08	62	0.7	4.0×10^{-8}	7.0×10^{-6}	-2.11 ± 0.20	28.1/33	—
GRB 040730	15:53:14	-56:28:15	51	0.32	3.4×10^{-8}	6.6×10^{-7}	-1.44 ± 0.14	34.3/33	—
GRB 040812	16:26:05	-44:42:32	16	0.7	5.0×10^{-8}	2.3×10^{-7}	-2.34 ± 0.29	19.5/26	X,R
GRB 040827	15:17:00	-16:08:21	35	0.42	6.0×10^{-8}	1.2×10^{-6}	-1.83 ± 0.18	32.5/29	X,O
XRF 040903	18:03:22	-25:15:23	15	0.23	2.0×10^{-8}	1.4×10^{-7}	-2.94 ± 0.44	16.6/20	—
GRB 041015	00:18:37	66:51:37	33	0.17	4.0×10^{-8}	6.0×10^{-7}	-0.95 ± 0.28	17.4/21	—
GRB 041218	01:39:06	71:20:05	40	3.19	2.8×10^{-7}	5.5×10^{-6}	Table 3	—	O
GRB 041219a ^m	00:24:26	62:50:06	186	33	3.6×10^{-6}	1.6×10^{-4}	Table 3	—	O,R
GRB 050129	16:51:12	-03:04:44	40	0.36	3.0×10^{-8}	4.5×10^{-7}	-1.91 ± 0.31	21.6/26	—
GRB 050223*	18:05:36	-62:28:26	39	0.67	6.0×10^{-8}	8.2×10^{-7}	-1.84 ± 0.25	21.3/30	X
GRB 050502a*	13:29:45	42:40:27	20	1.58	2.0×10^{-7}	$> 1.4 \times 10^{-6}$	Table 3	—	O,IR
GRB 050504	13:24:00	40:41:45	58	0.45	7.4×10^{-8}	1.3×10^{-6}	-1.32 ± 0.10	50.8/29	X
GRB 050520	12:50:03	30:27:02	80	0.53	4.0×10^{-8}	2.4×10^{-6}	-1.61 ± 0.07	26.1/30	X,R
XRF 050522	13:20:35	24:47:30	17	0.2	1.3×10^{-8}	7.0×10^{-8}	-2.72 ± 0.67	16.2/17	—
GRB 050525a*	18:32:33	26:20:23	12	31.7	3.1×10^{-6}	2.0×10^{-5}	Table 3	—	O,R
GRB 050626	12:26:58	-63:08:03	50	0.27	2.0×10^{-8}	7.6×10^{-7}	-2.20 ± 0.14	27.6/30	—
GRB 050714a	02:54:21	69:07:34	34	0.18	1.5×10^{-8}	4.7×10^{-7}	-2.06 ± 0.20	21.8/28	—
GRB 050918	17:50:26	-25:24:51	115	1.61	1.6×10^{-7}	3.1×10^{-6}	Table 3	—	—
GRB 050922a	18:04:37	-32:01:24	8	0.01	5.3×10^{-9}	5.3×10^{-8}	-1.85 ± 1.01	0.6/2	—
GRB 051105b	00:37:51	-40:28:52	16	0.31	3.0×10^{-8}	2.9×10^{-7}	-1.83 ± 0.23	25.7/27	—
GRB 051211b	23:02:45	55:04:44	60	0.6	6.1×10^{-8}	2.0×10^{-6}	-1.62 ± 0.10	38.4/28	X,R
GRB 060114	13:01:07	-04:44:53	63	0.31	3.0×10^{-8}	9.0×10^{-7}	-0.98 ± 0.16	18.9/30	—
GRB 060130	15:16:54	-36:54:43	29	0.11	7.7×10^{-9}	2.8×10^{-7}	-1.51 ± 0.40	27.7/22	—
GRB 060204a	15:28:56	-39:26:38	34	0.16	2.1×10^{-8}	6.6×10^{-7}	-1.43 ± 0.27	20.3/26	X
GRB 060428c ⁿ	19:00:52	-09:33:00	12	3.9	3.6×10^{-7}	2.3×10^{-6}	Table 3	—	—
GRB 060901 ^o	19:08:38	-06:38:22	20	8.6	9.0×10^{-7}	8.7×10^{-6}	Table 3	—	X,O
GRB 060912b	18:04:52	-19:52:50	91	0.08	8.8×10^{-9}	7.1×10^{-7}	-1.52 ± 0.23	18.5/33	—
GRB 060930 [†]	20:18:09	-23:37:31	20	0.3	2.2×10^{-8}	2.5×10^{-7}	—	—	—
GRB 061025	20:03:39	-48:14:39	11	1.14	1.3×10^{-7}	1.1×10^{-6}	Table 3	—	X,O
GRB 061122	20:15:21	15:30:51	11	31.7	3.1×10^{-6}	2.0×10^{-5}	Table 3	—	X,O
GRB 070309	17:34:44	-37:56:40	38	0.13	1.1×10^{-8}	5.4×10^{-7}	-1.73 ± 0.27	26.5/26	X?
GRB 070311 [†]	05:50:10	03:22:29	50	0.9	—	2.0×10^{-6}	—	—	X,O
GRB 070615	02:57:14	-04:24:28	27	0.41	2.8×10^{-8}	5.0×10^{-7}	-1.62 ± 0.28	21.9/27	—
GRB 070707	17:51:00	-68:52:52	0.8	1.72	2.1×10^{-7}	2.1×10^{-7}	-1.19 ± 0.14	51.2/47	X,O

^a Malaguti et al. (2003), ^b Mereghetti et al. (2003a), ^c Götz et al. (2003), ^d Mereghetti et al. (2003c), ^e von Kienlin et al. (2003a), ^f Beckmann et al. (2003), ^g Sazonov et al. (2004), ^h Moran et al. (2005), ⁱ McGlynn et al. (2005), ^j Mereghetti et al. (2005), ^k Filliatre et al. (2005), ^l Filliatre et al. (2006), ^m McBreen et al. (2006), ⁿ Grebenev & Chelovekov (2007), ^o A. von Kienlin (priv. comm.)

* 25–500 keV

* GRBs with known redshift; GRB 031203 at $z=0.106$ (Prochaska et al. 2004); GRB 050223 at $z=0.584$ (Pellizza et al. 2006); GRB 050502a at $z=3.793$ (Prochaska et al. 2005); GRB 050525a (Foley et al. 2005) at $z=0.606$.

[†] Data unavailable for GRB 060930 (values taken from Gotz et al. (2006)) and GRB 070311 (values taken from Mereghetti et al. (2007)).

Table 3. IBIS and SPI spectral properties of GRBs for which Band and quasithermal (PL + BB) models are fit to spectra. Parameters quoted are low energy power-law index, α , high energy power-law index, β , and break energy, E_0 , for Band model fits and temperature, kT and power-law index, Γ for quasithermal model fits.

GRB		Band Model				Quasithermal Model		
		α	β	E_0 (keV)	$\chi^2/d.o.f$	kT	Γ	$\chi^2/d.o.f$
GRB 030131	<i>IBIS</i>	-1.40 ± 0.20	-3.0 ± 1.0	70 ± 20	22.5/16	—	—	—
GRB 040422	<i>IBIS</i>	-1.26 ± 0.08	-3^\dagger	55 ± 31	42.0/35	14 ± 2	-2.49 ± 0.48	38.4/34
	<i>SPI</i>		-2.17 ± 0.28 (PL)		7.5/3	—	—	—
GRB 041218	<i>IBIS</i>	-1.15 ± 0.20	-2.08 ± 0.16	80 ± 40	64.4/35	14 ± 2	-1.76 ± 0.08	64.1/35
	<i>SPI</i>	-0.97 ± 0.47^1	-3^\dagger	116 ± 152	20.0/35	26 ± 9	-1.82 ± 0.38	19.4/34
GRB 041219a	<i>IBIS</i>	-1.67^\dagger	-1.92 ± 0.02	114 ± 144	184.0/157	30 ± 12	-2.03 ± 0.07	109.6/87
	<i>SPI</i>	-1.48 ± 0.08	-1.92 ± 0.13	365.9 ± 192	51.9/30	29 ± 3	-1.77 ± 0.03	17.6/18
GRB 050502a	<i>IBIS</i>	-0.89 ± 0.25	-3^\dagger	83 ± 44	34.7/38	17 ± 2	-1.64 ± 0.11	33.2/41
GRB 050525a	<i>IBIS</i>	-0.94 ± 0.45	-3^\dagger	65 ± 62	59.2/31	18 ± 4	-2.05 ± 0.58	60.1/31
	<i>SPI</i>	-1.37 ± 0.23	-3^\dagger	127 ± 45	46.9/51	26 ± 4	-2.24 ± 0.15	46.0/50
GRB 050918	<i>IBIS</i>	-1.42 ± 0.51	-3^\dagger	117 ± 1484	26.4/29	21 ± 5	-2.44 ± 1.22	23.8/28
	<i>SPI</i>	-1.28 ± 2.58	-3^\dagger	69 ± 890	4.4/7	15 ± 11	-2.24 ± 3.22	3.8/6
GRB 060428c	<i>IBIS/SPI</i>	-0.71 ± 0.26	-2.0	54 ± 14	32.3/33	—	—	—
GRB 060901	<i>IBIS</i>	-1.47 ± 0.20	-3^\dagger	998 ± 9002	40.2/30	36 ± 11	-1.91 ± 0.39	34.8/29
	<i>SPI</i>	-0.50 ± 0.61	-1.89 ± 0.42	85 ± 151	9.0/14	28 ± 11	-1.54 ± 0.15	14.0/14
GRB 061025	<i>IBIS</i>	-0.85 ± 0.43	-3^\dagger	94 ± 134	38.3/29	15 ± 6	-1.38 ± 0.30	35.6/28
	<i>SPI</i>		-1.57 ± 0.25 (PL)		10.4/6	17 ± 6	-0.75 ± 2.65	7.2/5
GRB 061122	<i>IBIS</i>	-0.97 ± 0.40	-2.00 ± 0.12	56 ± 52	47.4/30	12 ± 3	-1.72 ± 0.12	48.6/30
	<i>SPI</i>	-0.98 ± 0.12	-2.72 ± 0.85	166 ± 39	66.6/56	36 ± 3	-1.81 ± 0.08	67.8/56

 † Parameter frozen

Table 4. Spectral Lag Measurements for *INTEGRAL* GRBs. The columns refer to (from left to right): GRB; supergalactic longitude (SGL) and latitude (SGB); burst interval used in spectral lag determination relative to trigger time and as marked on time profiles in the Appendix; spectral lags measured between Channel 2 (50–100 keV) and Channel 1 (25–50 keV), $\tau_{2,1}$, Channels 2 and 3 combined (50–300 keV) and Channel 1 (25–50 keV), $\tau_{2+3,1}$ and Channel 3 (100–300 keV) and Channel 1 (25–50 keV), $\tau_{3,1}$.

GRB	SGL	SGB	Lag Interval	Spectral Lag		
				$\tau_{2,1}$ (s)	$\tau_{2+3,1}$ (s)	$\tau_{3,1}$ (s)
GRB 021219	29.91	73.72	29.5–33 s	0.33 ± 0.02	0.39 ± 0.01	0.63 ± 0.02
GRB 030320	-174.44	46.17	-5–50 s	0.08 ± 0.03	0.15 ± 0.03	0.28 ± 0.03
			5–20 s	0.33 ± 0.03	0.33 ± 0.03	0.28 ± 0.03
			37–49 s	-0.05 ± 0.03	0.05 ± 0.03	$0.28^{+0.05}_{-0.03}$
GRB 030501	-137.97	80.21	0–30 s	-0.30 ± 0.10	-0.25 ± 0.10	—
GRB 030529 [†]	178.44	-38.74	-5–16 s	0.30 ± 0.30	$0.40^{+0.20}_{-0.25}$	—
GRB 031203	178.37	-61.73	-5–20 s	$-0.05^{+0.04}_{-0.05}$	0.04 ± 0.03	$0.17^{+0.03}_{-0.04}$
GRB 040106	161.11	-22.05	-2–53 s	$0.00^{+0.10}_{-0.05}$	0.05 ± 0.05	—
			-2–10 s	$0.15^{+0.05}_{-0.10}$	$0.05^{+0.10}_{-0.05}$	—
			37–53 s	-0.35 ± 0.10	-0.30 ± 0.05	—
GRB 040223 ^{a †}	179.35	24.44	-15–15 s	$1.05^{+0.30}_{-0.35}$	$1.80^{+0.35}_{-0.25}$	—
GRB 040323 ^a	170.14	-3.73	0–20 s	$0.80^{+0.05}_{-0.10}$	$1.15^{+0.15}_{-0.05}$	$1.80^{+0.10}_{-0.20}$
GRB 040403 ^{a †}	30.70	-5.66	-10–10 s	0.60 ± 0.20	$0.95^{+0.25}_{-0.15}$	—
GRB 040422	-167.01	75.91	0–10 s	0.01 ± 0.01	0.01 ± 0.01	—
			2.5–4 s	-0.01 ± 0.01	-0.01 ± 0.01	—
			4–8 s	0.04 ± 0.01	$0.02^{+0.02}_{-0.02}$	—
GRB 040624 ^{b †}	120.23	0.26	-5–50 s	—	2.75 ± 0.20	—
GRB 040730 ^{c †}	-177.00	8.47	15–40 s	2.80 ± 0.50	$3.05^{+0.40}_{-0.45}$	$3.30^{+0.45}_{-0.35}$
GRB 040812	179.07	20.75	4–12 s	$-0.05^{+0.05}_{-0.10}$	-0.15 ± 0.10	—
			4–7.7 s	0.00 ± 0.05	$0.00^{+0.10}_{-0.15}$	—
			7.7–12 s	$-0.20^{+0.15}_{-0.10}$	$-0.30^{+0.15}_{-0.10}$	—
GRB 040827 ^{b †}	144.61	27.49	5–30 s	$3.15^{+0.20}_{-0.30}$	$4.85^{+0.15}_{-0.30}$	—
GRB 040903 [†]	-170.84	47.15	0–20 s	—	$\tau_{1,15-25} = 0.10^{+0.25}_{-0.15}$	—
GRB 041218	7.76	11.40	20–63 s	$0.05^{+0.02}_{-0.01}$	$0.04^{+0.01}_{-0.03}$	$-0.03^{+0.04}_{-0.02}$
			20–29 s	$0.24^{+0.06}_{-0.04}$	$0.15^{+0.05}_{-0.06}$	—
			31–40 s	$-0.01^{+0.02}_{-0.03}$	-0.02 ± 0.02	$-0.01^{+0.04}_{-0.02}$
			50–63 s	-0.02 ± 0.03	$-0.06^{+0.04}_{-0.02}$	—
GRB 041219a	-1.86	17.42	261–414 s	0.12 ± 0.02	0.15 ± 0.02	0.21 ± 0.02
			-1–7 s	$0.50^{+0.50}_{-0.08}$	$0.65^{+0.05}_{-0.06}$	$1.00^{+0.10}_{-0.09}$
			261–327 s	0.06 ± 0.02	0.08 ± 0.02	0.14 ± 0.02
GRB 050502a	75.87	16.88	356–414 s	0.10 ± 0.02	0.13 ± 0.03	0.18 ± 0.03
GRB 050502a	75.87	16.88	-16.5–-3.5 s	$-0.12^{+0.05}_{-0.08}$	-0.03 ± 0.06	$0.11^{+0.07}_{-0.06}$
GRB 050504 ^c	77.79	15.58	-5–60 s	$1.35^{+0.30}_{-0.20}$	$2.40^{+0.35}_{-0.25}$	$4.35^{+1.45}_{-0.70}$
GRB 050520	86.68	6.85	0–80 s	0.07 ± 0.02	0.07 ± 0.02	—
GRB 050522 [†]	93.81	12.17	0–20 s	—	$\tau_{1,15-25} = 0.70^{+0.15}_{-0.25}$	—
			2.5–6 s	—	$\tau_{1,15-25} = 0.80^{+0.75}_{-0.50}$	—
			7–16 s	—	$\tau_{1,15-25} = 0.70^{+0.15}_{-0.20}$	—
GRB 050525a	51.74	78.15	0–12 s	0.056 ± 0.001	0.069 ± 0.001	$0.130^{+0.003}_{-0.002}$
			0–4 s	0.053 ± 0.001	0.068 ± 0.001	$0.131^{+0.003}_{-0.002}$
			4–12 s	$0.066^{+0.003}_{-0.002}$	0.068 ± 0.002	$0.096^{+0.003}_{-0.005}$
GRB 050626 ^{c †}	178.46	-17.14	50–110 s	$3.35^{+0.45}_{-0.40}$	$3.25^{+0.35}_{-0.45}$	—
GRB 050918	-174.74	45.97	0–325 s	$0.17^{+0.04}_{-0.03}$	$0.17^{+0.03}_{-0.02}$	—
			0–50 s	$0.43^{+0.04}_{-0.05}$	$0.50^{+0.05}_{-0.04}$	—
			220–350 s	-0.06 ± 0.01	-0.14 ± 0.01	—
GRB 051211b ^b	-8.74	28.77	10–80 s	1.95 ± 0.35	$1.70^{+0.30}_{-0.35}$	$1.55^{+0.65}_{-0.35}$
GRB 060130 ^{c †}	163.67	16.50	-10–45 s	$4.05^{+0.15}_{-0.30}$	$3.45^{+0.35}_{-0.45}$	—
GRB 060901	-144.72	67.40	0–4 s	0.2 ± 0.1	0.2 ± 0.1	0.2 ± 0.1
GRB 061025	-140.43	24.19	-10–10 s	$0.35^{+0.10}_{-0.05}$	$0.40^{+0.05}_{-0.10}$	0.40 ± 0.05
GRB 070309 ^{a †}	-172.41	33.13	-25–10 s	—	$1.70^{+0.35}_{-0.30}$	—
GRB 070615 [†]	-59.34	-30.58	0–20 s	$0.70^{+0.25}_{-0.15}$	$0.40^{+0.15}_{-0.20}$	—
GRB 070707 [*]	-159.26	4.64	0.4–1.5 s	0.025 ± 0.005	0.005 ± 0.005	0.020 ± 0.005

^a Long-lag GRB in PCFoV to 50% coding. ^b Long-lag GRB in PCFoV outside 50% coding. ^c Long-lag GRB in FCFoV.

[†] Lag measured using wavelet-smoothed lightcurves.

* Short-duration GRB.

Table 5. Wavelet-denoised spectral lags of weak GRBs. The lags derived from raw data are shown for comparison where available. Spectral lags measured between Channels 2 and 3 combined (50–300 keV) and Channel 1 (25–50 keV), $\tau_{2+3,1}$, with the exception of the XRFs for which the lag is measured between 15–25 keV and 25–50 keV (Channel 1), $\tau_{1,15-25}$.

GRB	$\tau_{2+3,1}$ (raw data) (s)	$\tau_{2+3,1}$ (denoised data) (s)
GRB 030529	—	$0.40^{+0.20}_{-0.25}$
GRB 040223	$1.70^{+0.30}_{-0.25}$	$1.80^{+0.33}_{-0.25}$
GRB 040403	$1.05^{+0.55}_{-0.30}$	$0.95^{+0.25}_{-0.15}$
GRB 040624	$3.10^{+0.90}_{-0.30}$	2.75 ± 0.20
GRB 040730	$3.35^{+0.80}_{-0.55}$	$3.05^{+0.40}_{-0.45}$
GRB 040827	3.65 ± 0.30	$4.85^{+0.15}_{-0.30}$
XRF 040903	—	$\tau_{1,15-25} = 0.10^{+0.25}_{-0.15}$
XRF 050522	$\tau_{1,15-25} = 1.15^{+0.25}_{-0.45}$	$\tau_{1,15-25} = 0.70^{+0.15}_{-0.25}$
GRB 050626	$3.25^{+1.25}_{-0.65}$	$3.25^{+0.35}_{-0.45}$
GRB 060130	$3.65^{+1.00}_{-0.75}$	$3.45^{+0.35}_{-0.45}$
GRB 070309	—	$1.70^{+0.35}_{-0.30}$
GRB 070615	$0.40^{+0.15}_{-0.25}$	$0.40^{+0.15}_{-0.20}$

Table 6. Median properties of the 28 long-duration GRBs with a measured $\tau_{2+3,1}$, categorised into those with short lags ($\tau_{2+3,1} < 0.75$ s) and long lags ($\tau_{2+3,1} > 0.75$ s.)

	Short-lag GRBs	long-lag GRBs
Fraction of <i>INTEGRAL</i> GRBs	17/28	11/28
Median $\tau_{2+3,1}$ (s)	0.07	1.70
Median T_{90} (s)	27	50
Median F_{peak} (erg cm ⁻² s ⁻¹)	2.0×10^{-7}	4.0×10^{-8}
Median Fluence (erg cm ⁻²)	2.0×10^{-6}	7.6×10^{-7}
% within $\pm 30^\circ$ SGB	41%	91%

Appendix A: *INTEGRAL* Lightcurves

The lightcurves of 43 of the 47 *INTEGRAL* GRBs are presented in the 25–50 keV (dark lines) and 50–300 keV (light lines) energy bands. Exceptions are the XRFs which were not detected above 50 keV and for which the lightcurves are plotted in the 15–25 keV (dark lines) and 25–50 keV (light lines) and the very weak GRBs and GRBs with telemetry gaps for which a lag could not be determined which are given over the full energy range of 25–300 keV. The regions which were used in the spectral lag analysis are denoted by solid vertical lines and the temporal resolution is that at which the lag was determined. All lightcurve data is from the IBIS instrument on board *INTEGRAL* with the exceptions of GRB 041219a and GRB 050525a for which data is taken from the BAT instrument on *Swift* due to IBIS telemetry saturation. A satellite slew occurred during GRB 030131 and the lightcurve is not presented here but is available in Götz et al. (2003). GRB 060428c was discovered in the *INTEGRAL* archival data and the lightcurve is available in Grebenev & Chelovekov (2007). IBIS data is currently unavailable for GRB 060930 and GRB 070311.

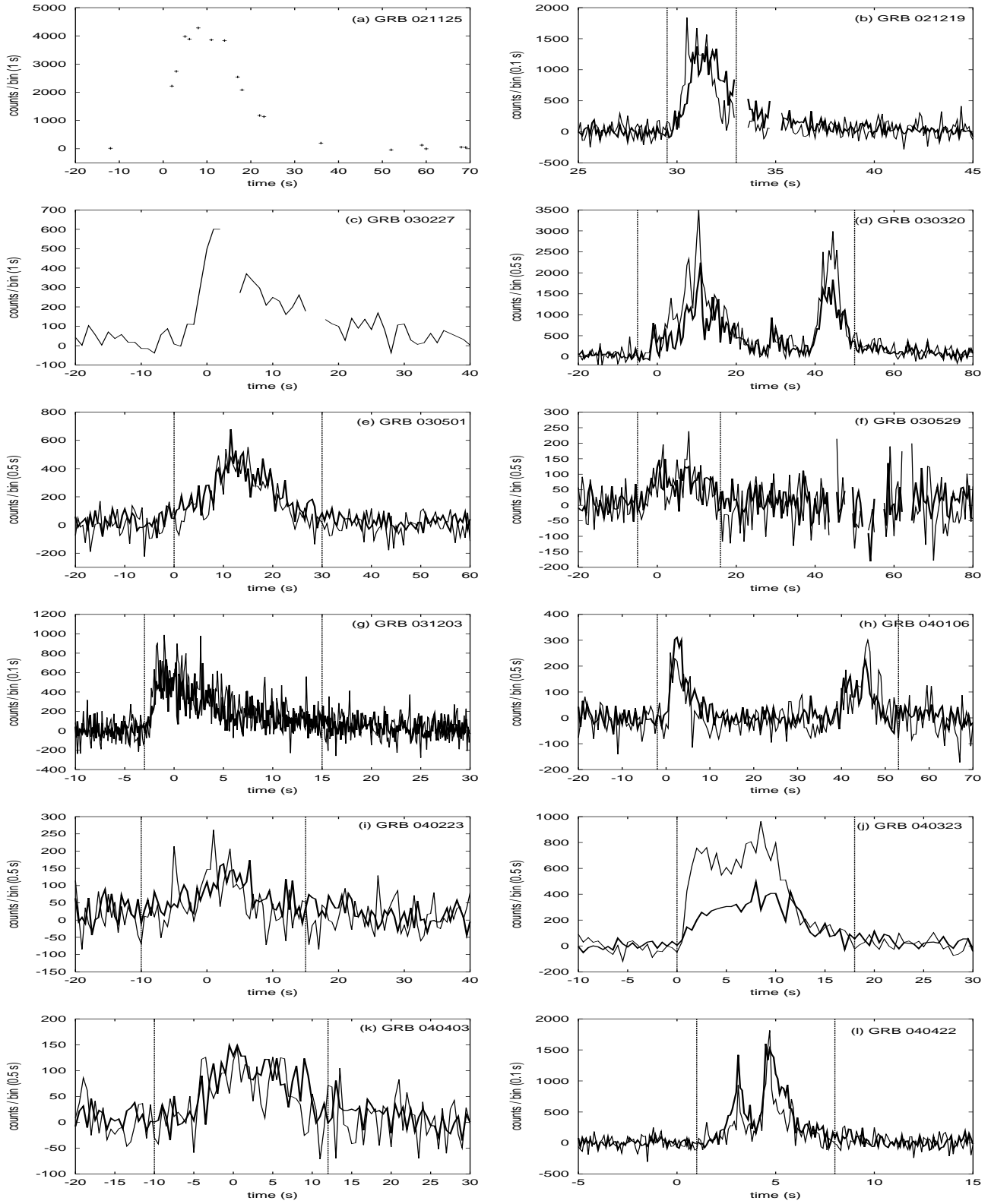
Fig. A.1. Lightcurves of GRBS observed with *INTEGRAL*.

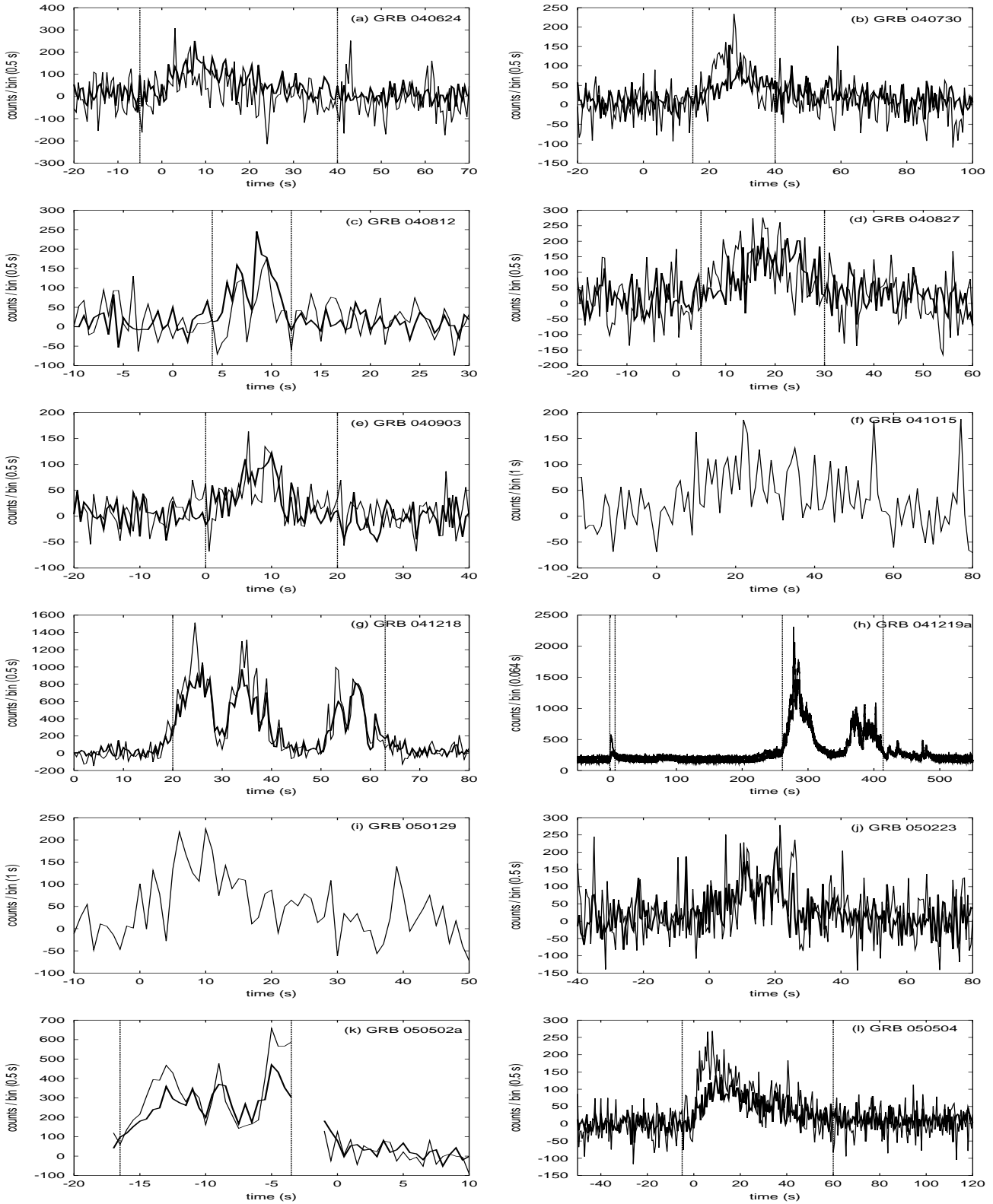
Fig. A.2. Lightcurves of GRBs observed with *INTEGRAL* (continued).

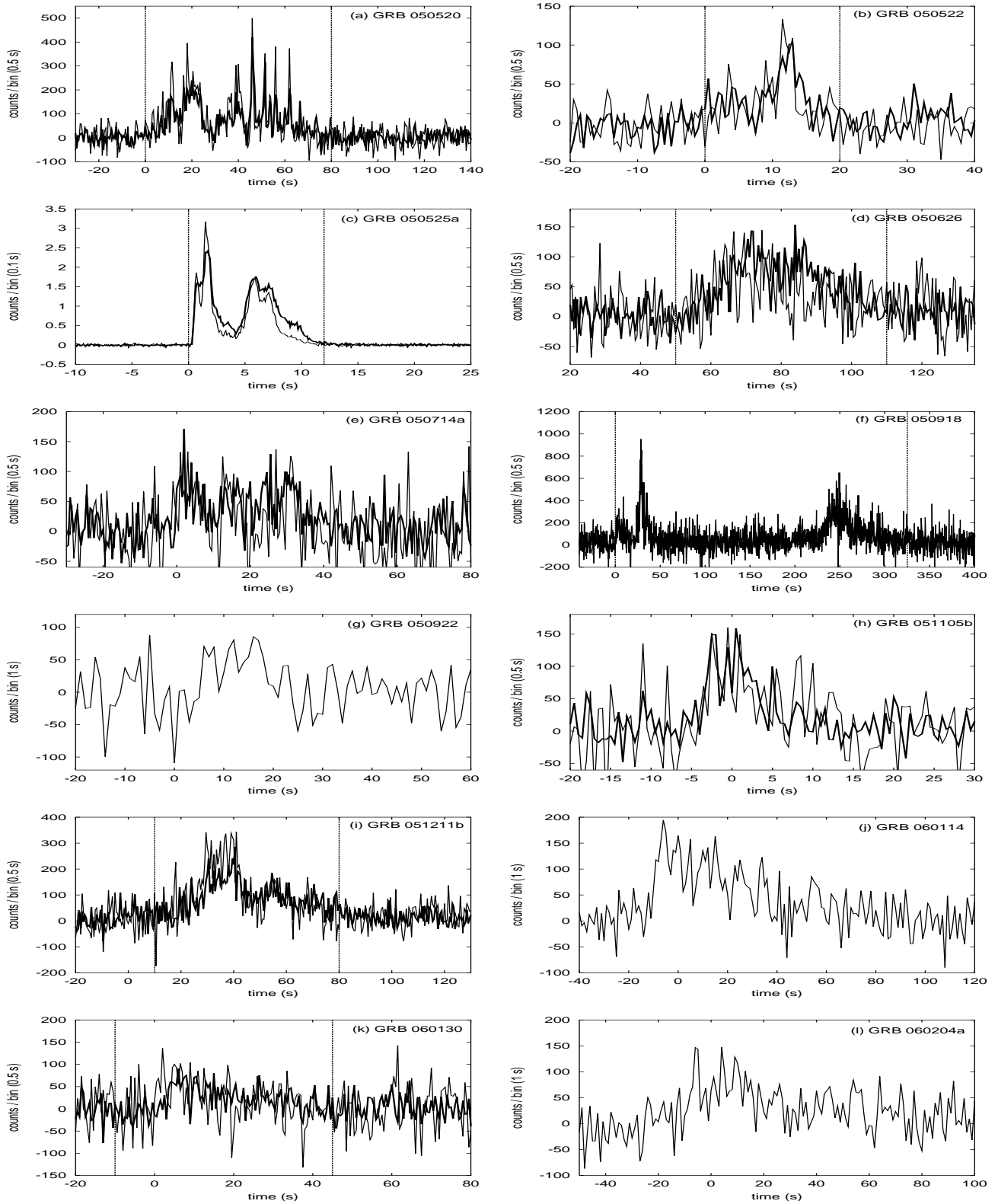
Fig. A.3. Lightcurves of GRBs observed with *INTEGRAL* (continued).

Fig. A.4. Lightcurves of GRBs observed with *INTEGRAL* (continued).